

Highly excited vibrational eigenstates of nonlinear triatomic molecules. Application to H₂O

Seung E. Choi and John C. Light
James Franck Institute, University of Chicago, Chicago, Illinois 60637

(Received 1 June 1992; accepted 24 July 1992)

Highly accurate quantum-mechanical calculations are presented for highly excited vibrational states of H₂O. The vibration Hamiltonian operator \hat{H}_{vib} for a nonlinear triatomic molecule is given in Radau coordinates. A direct product basis is chosen, and the \mathbf{H}_{vib} matrix is evaluated in the discrete variable representation (DVR) for the symmetrized Radau coordinates. Vibrational eigenstates are computed from the DVR \mathbf{H}_{vib} via the successive diagonalization/truncation technique. A comparison of the computed eigenvalues with those observed demonstrate the accuracy of our model. Highly excited vibrational states, up to 30 000 cm⁻¹ above the zero-point energy, are reported for the potential energy surface (PES) given by Jensen [*J. Mol. Phys.*, **133**, 438 (1989)]. Using natural orbital expansions, the eigenfunctions of vibrational states are analyzed to understand the origins of the dynamical mixing of the vibrational modes. The local/normal mode transitions, Fermi resonances, Darling–Dennison interactions, and the mode separabilities are investigated. Statistical studies on the energy level spacings are presented for two different types of PES.

I. INTRODUCTION

The widespread availability of tunable laser sources with narrow linewidth ($\Delta\nu < 0.001 \text{ cm}^{-1}$) has facilitated the measurement of ultrahigh-resolution absorption spectra of a variety of molecules in a wide range of energy levels.¹⁻³ Sensitive detection methods allow precise measurement of even highly excited vibrational states. Such experimental improvements make the efficient quantum calculation of highly excited molecular eigenfunctions and their energy levels very useful, particularly if the computed accuracies are comparable to the accuracy of the observed values, usually better than 0.1 cm^{-1} . Such calculations can be used to guide experimentalists to assign spectra, to extract accurate and useful information about the potential energy surfaces, to evaluate effects of spectroscopic “anomalies” due to interactions such as Fermi resonances and local mode degeneracies in high energy regions, and finally to study such concepts as “quantum manifestations of classical chaos.”

Needless to say, however, the problem of solving the Schrödinger equation for large amplitude vibration motion quickly becomes intractable as the size of a molecule increases. As the number of energy levels increases and the amplitudes of vibrational motions become large, a single set of orthogonal coordinates does not exist in which the internal motions are clearly uncoupled; the motion is no longer separable in any set of coordinates. Choosing the optimum coordinate system and the basis functions for each degree of motion becomes important in evaluating the accurate vibrational eigenstates over the full range of the coordinate space of interest.

In the past spectroscopists have developed analytical representations of energy levels based on perturbation theory and power series expansions of the potential energy

function about the equilibrium geometry.⁴ High order equations contain terms for vibrational mixings due to Fermi resonances and Darling–Dennison resonances. Such analytic modeling has provided the requisite qualitative information for assignment of molecular spectra, particularly for states which are not far from the equilibrium configuration. As molecular spectra of higher resolution over a wider range of energy become available, however, it becomes important to have a means of accurate theoretical prediction of energy levels in an extended energy range, while retaining as much as possible simple physical pictures of the dynamics of a molecule in highly excited states.

For quantum mechanical calculations of energy levels of small molecules, the variational approach is the most widely used. It has been successfully applied to systems such as LiCN,^{5,6} HCN,^{7,8} H₃⁺,⁹⁻¹⁴ etc. to treat the highly excited (floppy) vibrational states which lie above the barrier to different configurational isomers. The numerical procedures adapted to carry out variational computations, however, have only recently become efficient enough to evaluate energy levels of highly excited vibrational states of extremely anharmonic molecular systems, such as H₂O. In order to obtain the desired numerical accuracy (better than or comparable to the observed high resolution spectra), even more efficient and facile computational methods are desired.

The development of the discrete variable representation¹⁵⁻¹⁸ (DVR) has significantly enhanced the efficiency of numerical treatment of diverse quantum mechanical problems. Several of the most efficient and accurate computations of highly excited vibrational states of triatomic systems have been done incorporating the DVR in portions of computations. Because of the ease of evaluation of the vibration–rotation Hamiltonian, \mathbf{H}_{RV} , in the DVR, a good basis for each internal coordinate can be chosen from a

wide class of available mathematical functions. The sparse nature of the multidimensional \mathbf{H}_{RV} matrix in the DVR also makes this numerical approach extremely efficient. Since in a DVR the coordinate matrix is diagonal, any analytical form of the potential energy surface can be used effectively.

For obvious reasons water is one of the most widely studied molecules, both theoretically and experimentally. High resolution spectra of water vapor have been measured for pure vibrational states with energy levels as high as $\sim 25\,000\text{ cm}^{-1}$ (Refs. 19 and 20, and references therein). The observed states, however, do not include highly excited bending vibrational states. In this paper we use the DVR approach to study the vibrational states of H_2O to very high vibrational levels (to $\sim 30\,000\text{ cm}^{-1}$ above the zero-point energy). Accurate energy levels are evaluated, and their wave functions are analyzed to study the resonance interactions among different vibrational states. Two different potential energy surfaces (PES's) are used for comparisons.

For highly excited vibrational states, extensive mixing of the zeroth-order vibrational modes (e.g., normal modes) is apparent. The energy spacings of bending states range widely depending on whether the bending energy is below or above the barrier to linearization. Overlaps of Fermi resonances and local mode degeneracies become ubiquitous as the density of states increases. The statistical analysis for the energy level spacings is used to look for the "quantum manifestation of classical chaos."

This article is organized as follows: In the following section numerical methods are defined. A general form of the vibrational Hamiltonian, \hat{H}_{vib} , for a nonlinear triatomic molecule is derived in Radau coordinates. The \hat{H}_{vib} of a C_{2v} molecule is specifically given in symmetrized Radau coordinates. Section III contains our choice of (direct product) basis functions for the effective vibrational motions. Both the finite basis representation (FBR) and the DVR of the Hamiltonian matrix are presented. This section also contains evaluations of different potential energy surfaces available for the H_2O system, and our modifications of the PES's to force physically reasonable behavior. In Sec. IV computational results of accurate vibrational energies, with the normal mode assignments, for both symmetric and antisymmetric symmetry groups of H_2O are presented up to $\sim 27\,000\text{ cm}^{-1}$ above the zero-point energy. The computed energy levels are compared to the observed levels. The wave functions of H_2O in a wide range of energy levels provide qualitative information regarding the dynamical mixing of the vibrational modes. Discussions of various analyses on the states up to $\sim 30\,000\text{ cm}^{-1}$ are also presented in this section. Local mode characteristics of states and couplings of eigenstates due to Fermi resonances and Darling–Dennison resonances are studied. Separability in the symmetrized Radau coordinates (which are similar to the normal modes) is described in terms of natural orbital expansions. Statistical studies on the energy level spacing distributions are included for two different PES's. Section V contains our concluding remarks.

II. NUMERICAL METHODS

In this section we will first define the symmetrized Radau coordinate system and the body-fixed axes which we use. We then define the vibrational Hamiltonian operator, \hat{H}_{vib} , of a nonlinear triatomic molecule of C_{2v} symmetry. The basis functions are given in the DVR. Finally, we discuss the sequential diagonalization/truncation procedure used to solve the three-dimensional vibration problem.

A. Hamiltonian and coordinate systems

The internal valence coordinates (r_1, r_2, ρ) , which are specified as the two bond lengths and the angle between the bonds, are transformed to a set of orthogonal internal coordinates, such as Radau coordinates (R_1, R_2, θ) , to simplify the kinetic energy operator. Radau coordinates are convenient to use for triatomic molecules for which the central atom is heavier than the other two atoms.²¹ In such systems, Radau coordinates closely resemble the valence coordinates, and the two coordinate systems are related according to

$$\mathbf{R}_1 = (\mu + 1 - g) \cdot \mathbf{r}_1 + (g - 1) \cdot \mathbf{r}_2, \quad (1a)$$

$$\mathbf{R}_2 = (\mu - g) \cdot \mathbf{r}_1 + g \cdot \mathbf{r}_2, \quad (1b)$$

$$\cos \theta = \frac{\mathbf{R}_1 \cdot \mathbf{R}_2}{|\mathbf{R}_1 \cdot \mathbf{R}_2|}, \quad (1c)$$

where

$$\mu = \left(\frac{m_3}{m_1 + m_2 + m_3} \right)^{1/2},$$

$$g = \frac{m_1 + m_2 \mu}{m_1 + m_2},$$

in which m_1 and m_2 are the masses of the two end atoms, and m_3 denotes the mass of the center atom.

For symmetric (C_{2v}) triatomic systems, linear combinations of the mass-weighted Radau stretching coordinates (R_1, R_2) define symmetrized stretching coordinates (R, r) . With this symmetrization, the coordinates reflect the symmetry properties of the molecular vibrational motions under the specific σ -symmetry operation (of reflection through the molecular plane of symmetry). Thus R and r are symmetric and antisymmetric upon the exchange of (mass-weighted) R_1 and R_2 , respectively,

$$R = (R_1 + R_2) / \sqrt{2}, \quad (2a)$$

$$r = (R_1 - R_2) / \sqrt{2}. \quad (2b)$$

The symmetrized Radau coordinates strongly resemble the normal coordinates for C_{2v} systems. The vibrational Hamiltonian for a C_{2v} molecule in terms of the symmetrized Radau coordinates (R, r, θ) can be written as

$$\hat{H}_{\text{vib}}(R,r,\theta) = \hat{K}_R + \hat{K}_r + \hat{K}_\theta + \hat{V}(R,r,\theta), \quad (3)$$

in which $m = m_1 = m_2$ and

$$\hat{K}_R = \frac{-\hbar^2}{2m} \frac{\partial^2}{\partial R^2}, \quad (4a)$$

$$\hat{K}_r = \frac{-\hbar^2}{2m} \frac{\partial^2}{\partial r^2}, \quad (4b)$$

$$\hat{K}_\theta = \frac{-\hbar^2}{2I} \frac{1}{\sin \theta} \frac{\partial}{\partial \theta} \sin \theta \frac{\partial}{\partial \theta}, \quad (4c)$$

and

$$\frac{1}{I} = \frac{1}{mR_1^2} + \frac{1}{mR_2^2}. \quad (5)$$

The volume element is $d\tau = dR dr \sin \theta d\theta$, for the coordinate ranges of $0 \leq R < \infty$, $-\infty < r < \infty$, $0 \leq \theta \leq \pi$. The coordinates (R,r,θ) correspond to the symmetric stretching, antisymmetric stretching, and the bending motions.

B. The discrete variable representation

The optimal choice of basis functions depends on the type of internal coordinate system used, the potential energy surface, the number of accurate eigenvectors desired, and the method of solution of the Schrödinger equation. The efficiency and accuracy of a computation of eigenfunctions and eigenvalues are strongly dependent on the choice of the basis functions in which the Hamiltonian matrix is represented. We show in this section that with proper attention to the physics of the molecular system, basis functions can be chosen to have appropriate boundary conditions and to minimize the problems of the inherent singularities in the kinetic energy operators. Since the (diagonal) representation of the potential energy matrix is quite easy in the DVR, the basis functions may be chosen from a wide range of available analytic functions.

The general characteristics of our symmetrized Radau coordinate system are such that small values of the symmetric stretching coordinate R correspond to the three atoms close to each other, while large R will correspond to one of the possible dissociation configurations. Both large and small values of R lie in regions of very high potential energies, and the lower energy range of R is strongly dependent on angles. In a C_{2v} molecule, the $r=0$ configuration corresponds to the equilibrium structure and the potential energy surface is symmetric about $r=0$. The angle θ ranges from 0° at the O–H–H linear configuration to 180° at the linear H–O–H configuration. The potential energy function varies substantially in angle and has a single minimum well between these two (limiting) linear configurations.

However, it is clear from Eqs. (3) and (4a)–(4c) that the kinetic energy operators exhibit singular behavior at linear configurations, $\theta=0^\circ$ or 180° , and for $R_1=0$ or $R_2=0$.²² Although this is a natural consequence of the choice of this (and most) internal coordinate system, it has caused substantial problems and comment in earlier treat-

ments. In particular, discussions of approximate Hamiltonian formulations such as normal coordinate Hamiltonians, “rigid bender” Hamiltonians, etc. have been concerned about these terms. An appropriate basis and coordinate system will, however, minimize the problem of effective potential singularities and permit easy symmetrization to reflect the proper C_{2v} symmetry desired according to the boundary conditions. The boundary conditions and the nodal structures of the basis functions must be appropriate for the physical properties and the symmetry of the Hamiltonian operator in the specific internal coordinates.

Because of the strong asymmetry of the potential energy function, widely different coordinate R ranges are required at different angles. A globally appropriate range must include the absolute minimum and the absolute maximum R that are accessed over all angles. Under such circumstance, a uniform basis over the interaction coordinate range seems to be most appropriate for R . The normalized Chebychev (First kind) polynomials, $\{\mathcal{F}_j(R)\}$, which are shifted and scaled, can generate a DVR basis which yields an evenly spaced set of DVR points. Moreover, the DVR points lie within the specified coordinate range and therefore do not lie on the boundaries at which singularities may exist.

The symmetrization of Radau coordinates has generated a stretching coordinate r which carries the symmetry signature of the system. The equilibrium configuration of a C_{2v} molecule corresponds to $r=0$ about which the potential-energy surface is symmetric. Furthermore, a vibrational eigenstate of a C_{2v} molecule can be symmetric or antisymmetric about $r=0$. Utilizing such molecular symmetry the \mathbf{H}_{vib} matrix may be reduced to a block-diagonal structure. Harmonic oscillator functions, $\{\mathcal{H}_j(r)\}$, consist of symmetric and antisymmetric functions about $r=0$, for even and odd j , respectively. The harmonic basis of each symmetry may be transformed to the DVR to yield two half-sized DVR bases that correspond to different symmetries. Symmetric or antisymmetric vibrational eigenstates are expanded exclusively in terms of the basis with proper symmetry.

The potential energy surface of a C_{2v} molecule is quite asymmetric in the angle θ of Radau coordinates. Therefore, our basis should be flexible in order to adjust for the asymmetry of the potential about 90° . Jacobi polynomials, $\{\mathcal{P}_j^{(a,b)}(x)\}$, seem most suitable in this regard. The boundaries of the interaction range $[0,\pi]$ correspond to two different linear configurations. The parameter a of Jacobi polynomials is chosen to accommodate the asymmetry of the PES in θ , and b is determined according to the boundary condition as $\theta \rightarrow 180^\circ$. For pure vibrational states which must be symmetric about the $C_2(z)$ axis, the amplitude of φ_q^{vib} must be finite as $\theta \rightarrow 180^\circ$ which requires $b=0$. Since the potential-energy function is extremely repulsive as $\theta \rightarrow 0^\circ$, the parameter a can be adjusted to cover only the effective range of θ , for the given energy range.

The vibrational wave functions are now expanded in the direct product basis of Chebyshev polynomials, $\{\mathcal{F}_j(R)\}$; harmonic-oscillator functions, $\{\mathcal{H}_j(r)\}$; and

Jacobi polynomials, $\{\mathcal{F}_i^{(a,b)}(x)\}$, where $x = \cos \theta$. The direct product basis for a finite basis representation (FBR), $\{\psi_{lji}\}$, of the internal coordinates is written as

$$\psi_{lji}(R, r, \theta) = \mathcal{F}_l(R) \mathcal{H}_j(r) \mathcal{F}_i^{(a,b)}(x). \quad (6)$$

Since the evaluation of the vibrational Hamiltonian operator is computationally much more accurate and faster for the direct product basis in the DVR, $\{\chi_{\alpha\beta\gamma}\}$, the FBR basis is transformed to the DVR; namely,

$$\begin{aligned} \chi_{\alpha\beta\gamma}(R, r, \theta) &= \sum_{l,j,i} \mathbf{T}_{\alpha\beta\gamma}^{lji} \cdot \psi_{lji}(R, r, \theta) \\ &= \Gamma_\alpha(R) \Phi_\beta(r) \Theta_\gamma^{(a,b)}(x), \end{aligned} \quad (7)$$

in which the \mathbf{T} matrix is defined as the direct product of \mathbf{t} matrices for the three internal coordinates

$$\mathbf{T}_{\alpha\beta\gamma}^{lji} = \mathbf{t}_{l\alpha}^R \cdot \mathbf{t}_{j\beta}^r \cdot \mathbf{t}_{i\gamma}^\theta$$

and

$$\Gamma_\alpha(R) = \sum_l \mathbf{t}_{l\alpha}^R \cdot \mathcal{F}_l(R), \quad (8a)$$

$$\Phi_\beta(r) = \sum_j \mathbf{t}_{j\beta}^r \cdot \mathcal{H}_j(r), \quad (8b)$$

$$\Theta_\gamma^{(a,b)}(x) = \sum_i \mathbf{t}_{i\gamma}^\theta \cdot \mathcal{F}_i^{(a,b)}(x). \quad (8c)$$

Here, \mathbf{t}^R , \mathbf{t}^r , and \mathbf{t}^θ are the FBR–DVR transformation matrices for Chebyshev polynomials, harmonic oscillator functions, and Jacobi polynomials, respectively. The transformation matrices of Eqs. (8a)–(8c) are orthogonal, and are determined as the diagonalizing transformation for the appropriate coordinate matrices in the FBR. Thus, we have

$$\sum_\nu \mathbf{t}_{n'\nu} \mathbf{t}_{n\nu} = \delta_{n'n}, \quad (9a)$$

$$\sum_n \mathbf{t}_{n'\nu} \mathbf{t}_{n\nu} = \delta_{\nu'\nu}. \quad (9b)$$

In order to evaluate the \mathbf{t} -matrix elements, we look at the unique properties of coordinate matrices in the FBR, $\tilde{\mathbf{q}}$, and DVR, \mathbf{q} . The orthogonal transformation between FBR and DVR gives

$$\mathbf{q} = \mathbf{t}^T \cdot \tilde{\mathbf{q}} \cdot \mathbf{t}, \quad (10)$$

in which

$$\tilde{\mathbf{q}}_{n'n} = \int f_{n'}(q) \cdot q \cdot f_n(q) dq, \quad (11a)$$

$$\mathbf{q}_{\nu'\nu} = \int \phi_{\nu'}(q) \cdot q \cdot \phi_\nu(q) dq. \quad (11b)$$

$\{f_n\}$ and $\{\phi_\nu\}$ denote related FBR and DVR bases, respectively. \mathbf{t} is then defined as the eigenvector matrix of $\tilde{\mathbf{q}}$, and \mathbf{q} is the diagonal matrix of its eigenvalues; namely,

$$\mathbf{q}_{\nu'\nu} = q_\nu \cdot \delta_{\nu'\nu}. \quad (12)$$

The $\{q_\nu\}$ are defined as DVR points. From Eqs. (11b) and (12), it follows that the DVR basis functions are the eigenfunctions of the coordinate operator. Furthermore, the N -point Gaussian quadrature approximation to Eq. (11a) substituted into Eq. (10) gives

$$\mathbf{t}_{n\nu} = \sqrt{\omega_\nu} \cdot f_n(q_\nu) \quad (13)$$

in which $\{\omega_\nu\}$ are the Gaussian weights, $\{q_\nu\}$ are the Gaussian quadrature points, and $\{f_n\}$ denote a class of normalized orthogonal polynomials of the FBR with n specifying the order of a function.¹⁶

The DVR basis for coordinate r can be symmetrized to yield two half-sized bases, $\{^S\Phi_\beta(r)\}$ and $\{^A\Phi_\beta(r)\}$, which are symmetric and antisymmetric with respect to reflection about the molecular symmetry axis, respectively. The resulting DVR direct product basis of internal coordinates can, therefore, also be separated in terms of the symmetries of vibration eigenfunctions. The symmetrized DVR direct product basis, $\{^{(g)}\chi_{\alpha\beta\gamma}\}$, where $(g) = S$ or A , easily yields the very sparse \mathbf{H}_{vib} matrix of Eq. (3), which is block diagonal in symmetry,

$$\mathbf{K}_{\alpha'\alpha}^R \cdot \delta_{\beta'\beta} \cdot \delta_{\gamma'\gamma} \cdot \delta_{g'g} = \int \chi_{\alpha'\beta'\gamma'}^{(g')} \cdot \left(-\frac{\partial^2}{\partial R^2}\right) \cdot \chi_{\alpha\beta\gamma}^{(g)} d\tau, \quad (14a)$$

$$\delta_{\alpha'\alpha} \cdot \delta_{\beta'\beta} \cdot \delta_{\gamma'\gamma} \cdot \delta_{g'g} = \int \chi_{\alpha'\beta'\gamma'}^{(g')} \cdot \left(-\frac{\partial^2}{\partial r^2}\right) \cdot \chi_{\alpha\beta\gamma}^{(g)} d\tau, \quad (14b)$$

$$\begin{aligned} \mathbf{A}_{\alpha\beta} \cdot \delta_{\alpha'\alpha} \cdot \delta_{\beta'\beta} \cdot \mathbf{K}_{\gamma'\gamma}^\theta \cdot \delta_{g'g} \\ = \int \chi_{\alpha'\beta'\gamma'}^{(g')} \cdot \frac{\hbar^2}{2I} \left(-\frac{1}{\sin \theta} \frac{\partial}{\partial \theta} \sin \theta \frac{\partial}{\partial \theta}\right) \cdot \chi_{\alpha\beta\gamma}^{(g)} d\tau, \end{aligned} \quad (14c)$$

$$\mathbf{V}_{\alpha\beta\gamma} \cdot \delta_{\alpha'\alpha} \cdot \delta_{\beta'\beta} \cdot \delta_{\gamma'\gamma} \cdot \delta_{g'g} = \int \chi_{\alpha'\beta'\gamma'}^{(g')} \cdot \hat{V}(R, r, \theta) \cdot \chi_{\alpha\beta\gamma}^{(g)} d\tau, \quad (14d)$$

in which $d\tau = dR dr dx$, and $^{(g)}\mathbf{K}^r$ carries the signature of the molecular symmetry. The matrix element $\mathbf{A}_{\alpha\beta}$ in Eq. (14c) represents the $1/2I$ term, which is a function of (R, r) given by Eq. (5), evaluated at a DVR point (R_α, r_β) . The diagonal potential energy matrix \mathbf{V} has as its elements $\{V_{\alpha\beta\gamma}\}$ the potential energies evaluated at DVR points $\{R_{\alpha'} r_{\beta'} x_{\gamma'}\}$. The DVR kinetic energy matrices for the three internal coordinates, denoted by \mathbf{K}^R , $^{(g)}\mathbf{K}^r$, and \mathbf{K}^θ , are obtained by transforming the equivalent matrices from the FBR. (A further discussion of the \mathbf{K} matrices is presented in Appendix A.) Thus, the DVR \mathbf{H}_{vib} matrix is written as

$$\begin{aligned}
{}^{(g)}\mathbf{H}_{\alpha\beta\gamma}^{\alpha'\beta'\gamma'} &\equiv \langle \chi_{\alpha'\beta'\gamma'}^{(g)} | \hat{H}_{\text{vib}} | \chi_{\alpha\beta\gamma}^{(g)} \rangle \\
&= \frac{\hbar^2}{m} (\mathbf{K}_{\alpha'\alpha}^R \cdot \delta_{\beta'\beta} \cdot \delta_{\gamma'\gamma} + \delta_{\alpha'\alpha} \cdot {}^{(g)}\mathbf{K}_{\beta'\beta}^r \cdot \delta_{\gamma'\gamma}) \\
&\quad + \mathbf{A}_{\alpha\beta} \cdot \delta_{\alpha'\alpha} \cdot \delta_{\beta'\beta} \cdot \mathbf{K}_{\gamma'\gamma}^\theta + \mathbf{V}_{\alpha\beta\gamma} \cdot \delta_{\alpha'\alpha} \cdot \delta_{\beta'\beta} \\
&\quad \cdot \delta_{\gamma'\gamma}, \quad (15)
\end{aligned}$$

in which sparsity of the matrix is self-evident.

C. Diagonalization of the vibrational Hamiltonian

A wavefunction of the n th vibrational eigenstate of a system may be expanded in the direct product basis of the optimum DVR functions for internal coordinates,

$$\Psi_n(R, r, \theta) = \sum_{\alpha\beta\gamma} \mathcal{B}_{\alpha\beta\gamma}^n \chi_{\alpha\beta\gamma}(R, r, \theta), \quad (16)$$

which is evaluated for a specific vibrational symmetry. The method of successive truncation is used to simplify calculations of the vibrational states. This numerical method is extremely effective for evaluating eigenvectors and eigenvalues of a large multidimensional Hamiltonian matrix in the DVR, in which coupling occurs in each dimension separately. (Further details regarding the method is given in Ref. 23.)

The eigenvalue equation for the vibrational states in the DVR may be written as

$$\mathbf{H}_{\text{vib}} \cdot \mathbf{B} = \mathbf{B} \cdot \mathbf{E}_{\text{vib}}, \quad (17)$$

in which \mathbf{E}_{vib} is the diagonal eigenvalue matrix for vibrational energy levels, and eigenvector matrix \mathbf{B} contains the expansion coefficients of $\{\mathcal{B}_{\alpha\beta\gamma}^n\}$ in Eq. (16). In the DVR, the matrix elements $\{\mathcal{B}_{\alpha\beta\gamma}^n\}$ directly correspond to the amplitudes of the n th vibrational eigenfunction evaluated at the $(\alpha\beta\gamma)$ DVR points; namely,

$$\Psi_n(R_{\alpha}, r_{\beta}, \theta_{\gamma}) = \Omega_{\alpha\beta\gamma}^{-1} \cdot \mathcal{B}_{\alpha\beta\gamma}^n \quad (18)$$

where $\Omega_{\alpha\beta\gamma} = (\omega_{\alpha}\omega_{\beta}\omega_{\gamma})^{1/2}$, and $\{\omega_{\alpha}, \omega_{\beta}, \omega_{\gamma}\}$ denote the weights given in Eq. (13).

III. BASIS FUNCTIONS AND POTENTIAL-ENERGY SURFACES

Although H₂O has been studied extensively both experimentally and theoretically, the information pertaining to its potential energy surface at highly excited energy levels is still limited due to difficulties of investigating large-amplitude motions. Particularly unfavorable Franck-Condon factors have limited the information about highly excited bending states. Furthermore, the accuracies of existing potential surfaces are still uncertain in terms of the bending coordinate. Our purposes in demonstrating an efficient and accurate numerical method for computations of H₂O vibrational eigenstates are, therefore, twofold. First,

our calculated energy levels are compared with those that are experimentally measured. Although these measured states include only relatively low bending states, the accuracy of our surface and computational method will be demonstrated. Second, energy levels and various analyses of the wave functions are presented for highly excited bending and stretching states which range up to $\sim 40\%$ of the dissociation energy. These states have not been observed yet experimentally; however, we have focused in characterizing the known PES's and comparing the similarities as well as differences in their topological features for future experimental investigations.

A. Potential-energy surfaces

This section contains our comments on different H₂O potential energy surfaces which are available. Two types of PES's have been used in our computations, based on those of Carter and Handy (CH) and of Jensen (JN). Carter and Handy²⁴ have improved the surface that was originally generated from an anharmonic force-field calculation by Hoy, Mills, and Strey (HMS).⁴ Recently, Jensen¹⁹ has determined a more accurate PES of H₂O from the Morse-oscillator-rigid-bender internal dynamics (MORBID) program. The JN's surface has included additional energy levels observed for higher-lying stretching states.

HMS first carried out force-field calculations for the potential energy surface (PES) of H₂O up to quartic terms of a Taylor's expansion in displacements of internal coordinates. Various authors have made contributions to improve the HMS surface since then.²⁵⁻²⁷ Halonen and Carington²⁸ carried out variational vibrational calculations for energy levels of $J=0$ H₂O in which the Morse variable was used as the stretching coordinates. In their calculations force constants of the HMS PES were rederived in terms of Morse variables.

Despite many improvements, the potential surfaces generated from the force-field calculations obviously do not have accurate asymptotic (dissociation) behavior. Furthermore, the correct symmetry properties of the system are not explicitly imposed on the function. The variables $(\Delta r_1, \Delta r_2, \Delta \theta)$ are allowed to vary from $-\infty$ to $+\infty$ without being restricted by specific boundary conditions, such as a periodicity of the bending coordinate. Thus, the HMS surface itself cannot yield proper convergence in computations of highly excited states. These are mainly states of large-amplitude bend motions, with amplitude at the H-O-H ($\theta = \pi$) linear configuration.

In order to fix this artifact of the HMS surface as $\theta \rightarrow \pi$ Carter and Handy imposed the proper boundary condition

$$\left. \frac{\partial V}{\partial \theta} \right|_{r_1, r_2} = 0$$

at $\theta = \pi$. The modification restores a proper symmetry around $\theta \rightarrow \pi$; however, it adversely affects the PES in the vicinity of the O-H-H ($\theta = 0$) configuration. Repulsive forces between the two H atoms are somehow canceled out by the modification, and the potential between them be-

comes attractive even at small H–H distances relative to the H_2 equilibrium bond length. The asymptotic behavior for (O–H–H) linear configurations leading to the $H_2 + O$ limit is incorrect at higher energies, which are well above the $\theta = \pi$ barrier.

The basic characteristic of a Taylor's expansion limits the adequacy of the HMS surface for states involving large-amplitude motions which are still far short of the dissociation limits. Sorbie and Murrell (SM) have described a method of constructing analytical potentials which have proper asymptotic behavior at the dissociation limits. Since the SM surface has proper symmetry properties of the molecule, leading to correct asymptotic atom–diatom dissociation limits, it would be preferred for collision dynamical calculations involving H_2O . However, its accuracy around the equilibrium geometry falls far short of that of the HMS surface. The energy levels computed from SM's surface are not adequate for comparison to the observed high-resolution spectroscopic studies. Since our purpose was to demonstrate the accuracy of our method for variational computations, the SM surface was not appropriate.

Jensen's PES, which is obtained from MORBID, yields the most reliable calculated energies extending as high as eight stretching quanta ($\sim 25\,000\text{ cm}^{-1}$ above the zero-point energy). It is predicted to break down for highly excited stretching states and has a problem similar to that for CH's PES for $\theta \rightarrow 0$ at small H–H distances. In order to correct the unphysical behavior of these surfaces in the vicinity of the O–H–H ($\theta = 0$) configuration, we have included an additional repulsive term for the H–H interaction; namely,

$$V(r_1, r_2, \rho) = V^\theta + V_{\text{H-H}}, \quad (19)$$

in which V^θ is the original (unmodified) potential energy and

$$V_{\text{H-H}} = \sum_{i=1}^2 C_i \exp[-\alpha_i(r_{\text{HH}} - d_{\text{HH}})]$$

and

$$\alpha_i = \beta_i \cdot [1 - \tanh(\gamma_s R^2)] [1 - \tanh(\gamma_a r^2)],$$

$$d_{\text{HH}} = \delta \cdot r_{\text{HH}}^0,$$

in which C_i 's, β_i 's, γ_s , γ_a , and δ are constants given in Table I. r_{HH} is the H–H distance, and d_{HH} is a fraction of the equilibrium H_2 bond distance, r_{HH}^0 . The modification does not change the original CH and JN surfaces at large angles, and up to $\sim 18\,000\text{ cm}^{-1}$ above the zero-point energy in the vicinity of $\theta = 0$. It generates a proper repulsive wall for small H–H distances. The one-dimensional (1D) cuts of the JN PES's are presented in Fig. 1 as a function of r for the O–H–H ($\theta = 0$) configuration at $R = 1.4\text{ \AA}$. Unless specifically noted, the results presented in the following sections are computed from the modified JN PES.

TABLE I. Constants used in the modification of potential-energy surfaces of Carter and Handy, and Jensen.

C_1	50.0 cm^{-1}
C_2	10.0 cm^{-1}
β_1	22.0 \AA
β_2	13.5 \AA
γ_s	0.05 \AA^{-1}
γ_a	0.10 \AA^{-1}
δ	0.85

B. Basis sizes and convergence

Once the choice of the basis is made, the factors that govern the convergence of our variational calculation are the sizes of bases for each coordinate, energy cuts at each successive truncation, and the coordinate ranges included in the computation. In Table II, we have presented a brief summary of various convergence tests of our 3D calculations using JN's surface. On the right-hand side we list the number and maximum energies of vibrational states converged to a given accuracy.

A typical calculation is done using 22 Chebyshev (first-kind) polynomials for the symmetric stretching coordinate (R), 22 Hermite polynomials for the antisymmetric stretching coordinate (r), and 30 Jacobi polynomials in $x (\equiv \cos \theta)$ with $(\alpha, \beta) = (8, 0)$. We denote this as the (22,22,30) basis for (N_R, N_r, N_θ) . Since the H_2O potential-energy surface is not symmetric about $\theta = \pi/2$ in Radau coordinates, Jacobi polynomials are more suitable than associated Legendre functions. The value of α in Jacobi polynomials adjusts the minimum angle for the effective angle θ range; α can be chosen to maximize the convergence of a computation for a given basis size and the desired accuracy

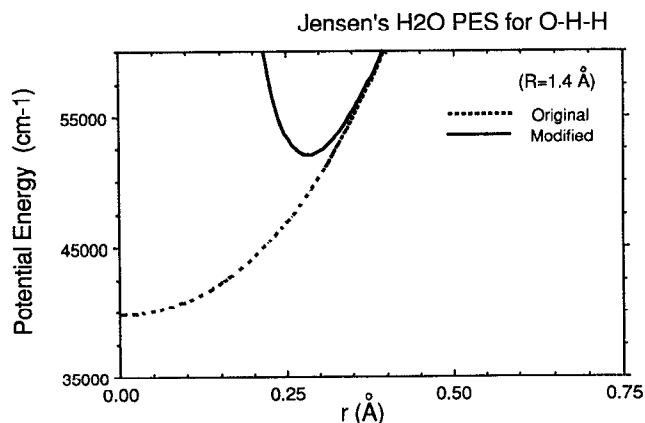


FIG. 1. The original and the modified Jensen potential energy surfaces are plotted for the O–H–H ($\theta = 0$) configuration as a function of r at $R = 1.4\text{ \AA}$. $r = 0$ corresponds to the case when the two H atoms are sitting on top of each other.

TABLE II. Convergence tests.

Input parameters						Convergences (cm^{-1})			
(N_R, N_r, N_θ)	R (\AA)	r (\AA)	(α, β)	$E2D_{\text{cut}}$	$N2D_{\text{min}}$	N_{H3D} (symm, asym)	$<0.01 \text{ cm}^{-1}$	$<0.05 \text{ cm}^{-1}$	$<0.20 \text{ cm}^{-1}$
(22,22,30)	[0.94,2.12]	[-0.65,0.65]	(8,0)	42 000	8	(966,846)	20 000 (133)	22 500 (186)	25 000 (252)
(30,30,30)	[0.92,2.20]	[-0.80,0.80]	(8,0)	45 000	8	(1182,1020)	22 500 (186)	25 000 (252)	27 800 (341)
(30,30,45)	[0.90,2.25]	[-0.75,0.75]	(10,0)	45 000	8	(1752,1539)	22 500 (186)	26 000 (270)	29 000 (417)
(35,34,60)	[0.92,2.30]	[-0.80,0.80]	(8,0)	43 000	8	(1986,1728)	22 500 (186)	25 000 (252)	27 400 (323)
(35,34,45)	[0.90,2.35]	[-0.85,0.85]	(5,0)	48 000	8	(2040,1815)	27 000 (313)	29 700 (412)	31 700 (502)

of the highest excited bend state. In contrast to the sharply repulsive behavior of the PES for $\theta \rightarrow 0$, the energy barrier to the H–O–H ($\theta \rightarrow \pi$) linear configuration, E_b , is fairly low. For the equilibrium O–H bond lengths, E_b is $\sim 12\,500 \text{ cm}^{-1}$ at $\theta = \pi$. $\beta = 0$ allows finite amplitudes at $\theta = \pi$ for highly excited bending states (above the barrier). Advantages of Jacobi polynomials over associated Legendre functions become more crucial for calculations of nonzero rotational states. Our work on $J > 0$ rovibrational states of H_2O is currently in preparation for publication.

The sequential diagonalization/truncation (SDT) method^{23,29,30} has been used to generate the final 3D-vibrational Hamiltonian matrix, evaluated in the 2D-eigenvector basis. First, a 1D-eigenvector basis is computed for every positive r and every third θ DVR point. Since the PES is symmetric about $r=0$, only half of the r -DVR points are unique. The PES is not a rapidly varying function in θ ; consequently, a 2D-eigenvector basis evaluated at a given DVR point is a good approximation for its nearest-neighbor θ points. Therefore, for each of the $(N_r/2) \times (N_\theta/3)$ (r, θ) -DVR points, the $N_R \times N_R$ 1D Hamiltonians are diagonalized, and the N_R eigenvectors are then truncated to a smaller number $P_{1D}(\beta, \gamma)$, according to an energy cutoff, E_{1D} (usually $90\,000 \text{ cm}^{-1}$). The number kept, $P_{1D}(\beta, \gamma)$, will be different for different (r_β, θ_γ) -DVR points.

In symmetrized internal (Radau) coordinates, the 2D Hamiltonian is block diagonal. Furthermore, 2D calculations can be carried out separately for stretching states of each symmetry. The block-diagonalized 2D Hamiltonian in DVR is then transformed to the truncated 1D-eigenvector basis, which forms much more efficient and accurate basis. Compared to the DVR basis size for the 2D Hamiltonian, which is $N_R \times (N_r/2) = 242$, the actual sizes $N_{2D}(\gamma) = \sum_\beta P_{1D}(\beta, \gamma)$ range between 140 and 165. At every third θ -DVR point, the 2D eigenvectors are evaluated and then truncated according to the energy cut, E_{2D} (usually $43\,000 \text{ cm}^{-1}$). For low bending states (even with highly excited stretching states), truncation of the 2D eigenvectors according to the energy criteria is much more effective than saving a fixed number of 2D eigenvectors.

For convergence of highly excited bending states, however, an extra constraint was used in order to generate the most efficient 2D-eigenvector basis. For small θ 's, the po-

tential energy surface has characteristics of a weakly bound system. As the H–O–H angle decreases the molecule starts to explore a much wider range of stretching configurational space, and the floppiness of molecules induces extensive mixing between stretching and bending coordinates. Truncation using a strict energy criterion does not provide a sufficient number of 2D-stretching eigenvectors for good convergence of the 3D-vibrational states involving highly excited bending states. Thus, we keep a minimum number P_{2D}^{min} of 2D eigenvectors at every θ -DVR point. In Table III we compare the convergence of two calculations, one of which is obtained using a strict energy cut and the other using the additional $P_{2D}^{\text{min}} = 8$ constraint with a little lower energy cut. The 3D Hamiltonian in DVR is finally transformed to the truncated 2D-eigenvector basis for each symmetry. A 2D-eigenvector basis is used for three consecutive θ 's, which include the one at which the 2D eigenvectors are generated and its two nearest-neighbor DVR points. Because of the SDT procedure, N_{3D} , the size of the 3D Hamiltonian in the 2D-eigenvector basis of a given symmetry, is much less than the DVR basis size $N_R \times (N_r/2) \times N_\theta$. For example, an initial basis of 7260 functions may be reduced to less than 1000.

The effects of varying basis size, energy cuts, and $N2D_{\text{min}}$ are shown in Table II, which gives the relevant sizes and the maximum energies and numbers of states converged to a given level. The convergence is checked against energy levels computed from $(N_R, N_r, N_\theta) = (30, 30, 45)$, $E1D_{\text{cut}} = 100\,000 \text{ cm}^{-1}$, $E2D_{\text{cut}} = 49\,000$

TABLE III. Convergence tests.

	$N2D_{\text{min}}$	$E3D_{\text{cut}}$	N_{H3D}	Convergence	
				(cm^{-1})	
				$<0.05 \text{ cm}^{-1}$	$<0.20 \text{ cm}^{-1}$
Symm	0	42 500	948	19 800 (80)	21 300 (96)
	8	41 000	927	22 500 (111)	25 000 (148)
Asym	0	42 500	798	22 300 (73)	24 600 (98)
	8	41 000	783	22 500 (75)	25 000 (104)

cm^{-1} , and $N2D_{\text{min}}=10$, which results in $N_{3\text{D}}=2136$ and 1884 for symmetric and antisymmetric states, respectively. The results are summarized in Table II.

IV. RESULTS AND DISCUSSIONS

The nature of energy flow within polyatomic molecules is an important factor controlling chemical kinetics. Investigations of energy flow based on classical mechanics and the theory of chaos in small systems have given considerable insight. Classically, chaotic dynamics and global energy flow may arise from the overlapping of various resonances.³¹ Much less is known, even classically, about the fully coupled dynamics of multidimensional vibrating molecules. Quantum mechanical studies based on perturbation theory and statistical models like those first evolved in nuclear physics have been carried out in order to characterize the dynamical properties of the vibrational and rovibrational energy level structure of H_2O .

Accurate calculations of highly excited vibrational states reveal detailed characteristics of the PES. The normal modes can be assigned by analyzing the nodal patterns of wave functions. The assignments are made following the most conventional notation, noted by $(\nu_1\nu_2\nu_3)$ with ν_1 = symmetric stretch, ν_2 = bend, and ν_3 = antisymmetric stretch. In case of states which are strongly mixed by resonances, the expectation values for $\langle R^2 \rangle$, $\langle r^2 \rangle$, and $\langle \cos^2 \theta \rangle$ are used as a guide to make proper assignments.

Based on the simple model studies for the correspondence between normal modes and local modes, the degeneracies are examined for local-mode pairs. Our analysis shows that the energy levels at which the normal to local mode transitions occur are strongly dependent on the magnitude of $\nu_1 + \nu_3$ and the extent of mixing between ν_1 and ν_2 . The effects of mode mixings on the resonances are discussed. The entropies of mixing, which are evaluated from the natural orbital expansion analysis, demonstrates the separabilities of vibrational modes. For states of low ν_2 the entropies are quite small even at high energies. The qualitative changes in energy level spacings and pattern of mode mixings are studied as the bending energy increases beyond the barrier to linearity (H-O-H). The statistical evaluations of energy level spacing distributions are presented in order to demonstrate the differences in the topological characteristics of the JN and CH potential energy surfaces.

In the following section we present the actual computational results for the modified JN and CH potentials and, where possible, compare with experiment. This shows that both surfaces yield quite good fits of known energy levels up to some $18\,000\text{ cm}^{-1}$ above zero point, and thus constitute quite reasonable bases for analysis of the vibrational behavior of higher energies. We then examine these sets of states with respect to local/normal mode behavior, separability of normal modes via natural orbital expansion, a brief look at the role of Fermi resonances, and finally the energy level spacing distributions. As will be seen, the overall picture, at least up to $30\,000\text{ cm}^{-1}$ above the zero point, is not adequately characterized by any of the simple models.

A. Accuracy of the computational model

The lowest 100 ($J=0$) states of the computed 3D-vibrational energy levels are given in Table IV for both modified JN and CH PES's and are compared with observed values, where available. Table V contains energy levels of highly excited stretching states that have been observed experimentally.¹⁹ With the same input parameters, calculations are also carried out for the original (e.g., unmodified) PES's. The results were within the $\pm 0.01\text{ cm}^{-1}$ of the tabulated values. The energy levels listed in Tables IV and V are converged to $\leq 0.005\text{ cm}^{-1}$, and the computation is carried out for the (22,22,30) basis which is reduced to $N_{3\text{D}}=(600,400)$ via the SDT according to $E2D_{\text{cut}}=40\,000\text{ cm}^{-1}$ and $P_{2\text{D}}^{\text{min}}=8$. Our computed vibrational energy levels of the modified CH and JN PES's are slightly different from those published by Fernley, Miller, and Tennyson.³² Their normal mode assignments also occasionally differ from ours.

The accurate energy levels of highly excited states are listed in Tables VI and VII for the modified JN surface. The tabulated values are converged to better than 0.05 cm^{-1} , and the assignments are given in normal-mode representation. The normal mode assignments are made by simply counting the nodes of the eigenvectors evaluated in the DVR. The 3D eigenvectors in symmetrized Radau coordinates are good approximations to the wave functions in normal coordinates. In general, the DVR eigenvectors are equal to the true wave functions evaluated at the DVR points times analytically known weight factors. The expectation values for $\langle R^2 \rangle$, $\langle r^2 \rangle$, and $\langle \cos^2 \theta \rangle$ are computed using the eigenvectors.

A large portion of the PES for H_2O is still not accurately known due to a lack of experimental information for bending states of $\nu_2 \geq 4$ for nonzero ν_1 or ν_3 states, and most of stretching states $(\nu_1 + \nu_3) \geq 6$. In Tables VI and VII, however, we have given accurate energy levels and their normal-mode assignments up to $27\,000\text{ cm}^{-1}$ for the (model) PES of H_2O . This information is useful in analyzing the various resonance features, as well as their effect on transitions from normal to local mode basis according to the given PES. The characteristics and the extent of the dynamical mixings of the zeroth-order (normal) vibrational modes can also be demonstrated.

B. Transition from normal mode to local mode

Local modes for systems with a heavy central atom were proposed by Lehmann and others and have been intensively investigated, particularly for two (stretch) mode models.³³⁻³⁵ In the strict local mode limit, the coupling between the bond oscillators is zero. The larger the mass of the central atom (in comparison to the end atoms), the weaker the kinetic coupling between the two bonds. Classically, a tunneling time between excitation of the two bonds may be related to the splitting between the two degenerate normal mode states of differing symmetry. The Darling-Dennison (DD) resonances, which couple $(\nu_1\nu_3)$ and $(\nu_1 \pm 2\nu_3 \mp 2)$ states, are analyzed in terms of excitations in stretch modes. The mixing of normal modes via the

TABLE IV. Lowest 100 vibrational energy levels of H₂O of either symmetry computed from the modified JN and CH surfaces. The computed energy levels are compared to those observed. Energies are given in cm⁻¹, and are measured from the ground vibrational states (0,0,0) $E=4636.455$ and 4630.350 cm⁻¹ for the CH and JN surfaces, respectively.

(ν_1, ν_2, ν_3)	E_{obs}^* ^a	$\Delta E_{\text{CH}}^\dagger$	$\Delta E_{\text{JN}}^\ddagger$	(ν_1, ν_2, ν_3)	E_{obs}^* ^a	$\Delta E_{\text{CH}}^\dagger$	$\Delta E_{\text{JN}}^\ddagger$
(0 1 0)	1594.747	0.655	-0.428	(0 7 1)	...	13 801.350	13 799.253
(0 2 0)	3151.631	0.331	0.380	(2 0 2)	13 828.3	12.136	1.424
(1 0 0)	3657.054	-0.733	-0.569	(3 0 1)	13 830.922	10.129	1.127
(0 0 1)	3755.924	0.319	0.011	(1 2 2)	13 910.8	-21.608	0.914
(0 3 0)	4666.808	-1.316	0.889	(0 2 3)	14 066.193	-8.363	9.801
(1 1 0)	5234.985	-0.527	-0.700	(4 0 0)	14 221.143	-10.760	2.354
(0 1 1)	5331.241	1.300	0.826	(1 0 3)	14 318.802	-17.519	2.699
(0 4 0)	6134.03	-4.852	0.090	(0 0 4)	14 536.87	-5.156	4.454
(1 2 0)	6775.095	-3.123	-0.074	(2 5 0)	...	14 556.170	14 549.224
(0 2 1)	6871.521	1.062	1.954	(1 5 1)	14 640	-15.253	-9.717
(2 0 0)	7201.54	2.815	1.127	(1 8 0)	...	14 760.300	14 778.301
(1 0 1)	7249.822	-1.016	1.121	(0 5 2)	...	14 840.392	14 858.931
(0 0 2)	7445.07	-2.441	-0.124	(0 8 1)	...	14 932.060	14 932.744
(0 5 0)	...	7531.431	7539.806	(3 3 0)	15 107	-9.664	2.671
(1 3 0)	8273.977	-7.499	-0.734	(2 3 1)	15 119.026	-14.127	3.565
(0 3 1)	8373.848	-0.518	1.801	(0 11 0)	...	15 180.972	15 181.417
(2 1 0)	8761.579	2.400	1.288	(2 1 2)	15 344.499	16.193	5.670
(1 1 1)	8807.002	-0.884	2.596	(3 1 1)	15 347.949	8.420	7.346
(0 6 0)	...	8849.971	8863.226	(1 3 2)	...	15 341.740	15 377.063
(0 1 2)	9000.140	-2.649	2.007	(0 3 3)	...	15 521.627	15 545.301
(1 4 0)	...	9711.739	9719.763	(4 1 0)	15 742.787	-16.324	1.300
(0 4 1)	9833.58	-4.159	-0.981	(2 6 0)	...	15 842.397	15 809.300
(0 7 0)	...	10 053.986	10 073.849	(1 1 3)	15 832.757	-22.490	6.345
(2 2 0)	10 284.4	-3.080	1.339	(1 6 1)	...	15 943.557	15 922.756
(1 2 1)	10 328.72	-4.255	3.689	(1 9 0)	...	15 948.181	16 023.707
(0 2 2)	10 524.3	-6.823	1.307	(0 1 4)	...	16 036.006	16 057.600
(3 0 0)	10 599.66	8.682	3.113	(0 9 1)	...	16 074.689	16 108.231
(2 0 1)	10 613.41	3.342	2.191	(0 6 2)	...	16 175.213	16 187.037
(1 0 2)	10 868.86	-11.937	0.466	(3 4 0)	...	16 511.609	16 525.427
(0 0 3)	11 032.4	-2.847	1.711	(2 4 1)	...	16 521.346	16 541.190
(1 5 0)	...	11 087.290	11 082.283	(0 12 0)	...	16 678.219	16 654.451
(0 8 0)	...	11 200.885	11 234.379	(1 4 2)	...	16 759.865	16 784.274
(0 5 1)	...	11 232.105	11 235.226	(3 2 1)	16 821.635	-3.673	2.235
(2 3 0)	...	11 756.656	11 766.215	(2 2 2)	16 825.23	-5.264	0.837
(1 3 1)	11 813.19	-9.555	2.287	(3 0 2)	16 898.42	16.389	1.089
(0 3 2)	...	12 000.803	12 011.521	(2 0 3)	16 898.842	16.026	0.739
(3 1 0)	12 139.2	7.801	5.261	(0 4 3)	...	16 948.038	16 974.657
(2 1 1)	12 151.26	2.665	5.272	(2 7 0)	...	17 087.179	17 054.741
(1 6 0)	...	12 363.878	12 340.755	(1 7 1)	...	17 186.869	17 156.820
(1 1 2)	12 407.64	-14.845	0.774	(4 2 0)	17 227.7	-31.144	-1.634
(0 9 0)	...	12 458.406	12 504.089	(1 10 0)	...	17 207.477	17 312.440
(0 6 1)	...	12 565.805	12 567.072	(1 2 3)	17 312.539	-31.886	7.789
(0 1 3)	12 565.0	-5.022	6.369	(0 10 1)	...	17 323.928	17 374.853
(2 4 0)	...	13 185.600	13 195.805	(0 7 2)	...	17 430.798	17 434.882
(1 4 1)	13 256	-16.298	-3.454	(5 0 0)	17 458.354	-8.190	-1.202
(0 4 2)	13 448	-5.010	5.603	(4 0 1)	17 495.528	-20.696	1.504
(1 7 0)	...	13 625.418	13 604.841	(0 2 4)	...	17 508.957	17 542.433
(3 2 0)	13 642	-0.472	5.746	(1 0 4)	17 748.073	-30.377	6.459
(2 2 1)	13 652.65	-4.486	6.073	(3 5 0)	...	17 877.326	17 877.874
(0 10 0)	...	17 756.449	13 793.447	(2 5 1)	...	17 891.515	17 903.164

^a E_{obs}^* denotes the observed energy levels given in Ref. 19. $\Delta E_{\text{CH}}^\dagger = E_{\text{CH}} - E_{\text{obs}}^*$, and $\Delta E_{\text{JN}}^\ddagger = E_{\text{JN}} - E_{\text{obs}}^*$, in which E_{CH} and E_{JN} are the vibrational energy levels computed using the modified potential energy surfaces of CH and JN, respectively.

TABLE V. Energy levels of highly excited stretching states compared to those observed. Energies are given in cm^{-1} .

(ν_1, ν_2, ν_3)	E_{obs}^* ^a	$\Delta E_{\text{CH}}^{\dagger}$	$\Delta E_{\text{JN}}^{\ddagger}$
(3 3 1)	18 265.820	-13.988	-4.863
(3 1 2)	18 392.974	12.540	10.995
(2 1 3)	18 393.314	12.010	11.520
(4 1 1)	18 989.961	-28.945	6.440
(3 4 1)	19 640	7.593	27.215
(3 0 3)	19 781.104	5.113	-23.786
(2 0 4)	19 782	4.303	-24.922
(5 0 1)	20 543.137	-19.496	-0.922
(2 1 4)	21 221.569	-6.527	-16.680
(3 1 3)	21 221.828	-6.820	-15.998
(3 0 4)	22 529.3	7.546	-52.341
(2 0 5)	22 529.445	7.377	-53.395
(3 0 5)	25 118.428	12.714	-83.102

^a E_{obs}^* denotes the observed energy levels in Ref. 19. $\Delta E_{\text{CH}}^{\dagger} = E_{\text{CH}} - E_{\text{obs}}$, and $\Delta E_{\text{JN}}^{\ddagger} = E_{\text{JN}} - E_{\text{obs}}$, in which E_{CH} and E_{JN} are the vibrational energy levels computed using the modified potential energy surfaces of CH and JN, respectively.

TABLE VI. Symmetric vibrational energy levels of H_2O calculated using the JN surface. Energies are given in cm^{-1} .

n	(ν_1, ν_2, ν_3)	E_{JN}^{\ddagger} ^a	n	(ν_1, ν_2, ν_3)	E_{JN}^{\ddagger} ^a	n	(ν_1, ν_2, ν_3)	E_{JN}^{\ddagger} ^a
63	(1 5 2)	18 119.682	109	(6 1 0)	22 390.827	155	(0 8 4)	25 540.069
64	(0 13 0)	18 172.311	110	(3 0 4)	22 476.959	156	(2 4 4)	25 557.286
65	(2 8 0)	18 257.331	111	(4 6 0)	22 579.531	157	(0 3 6)	25 601.052
66	(2 3 2)	18 272.006	112	(2 2 4)	22 631.902	158	(5 6 0)	25 729.910
67	(3 1 2)	18 403.969	113	(3 9 0)	22 743.592	159	(1 1 6)	25 760.401
68	(0 8 2)	18 566.852	114	(0 1 6)	22 755.725	160	(2 9 2)	25 858.184
69	(4 3 0)	18 665.045	115	(3 4 2)	22 776.684	161	(0 18 0)	25 941.090
70	(1 11 0)	18 684.665	116	(0 16 0)	22 839.815	162	(1 6 4)	26 046.813
71	(5 1 0)	18 958.419	117	(1 9 2)	22 956.803	163	(4 0 4)	26 097.334
72	(0 3 4)	18 995.916	118	(0 6 4)	23 104.239	164	(4 4 2)	26 180.276
73	(3 6 0)	19 148.224	119	(1 14 0)	23 168.743	165	(4 9 0)	26 203.484
74	(1 1 4)	19 250.689	120	(5 4 0)	23 210.006	166	(1 16 0)	26 233.960
75	(1 6 2)	19 376.422	121	(5 0 2)	23 380.846	167	(5 2 2)	26 337.832
76	(2 9 0)	19 493.063	122	(2 12 0)	23 446.463	168	(2 14 0)	26 374.158
77	(2 4 2)	19 664.822	123	(4 2 2)	23 468.011	169	(2 1 6)	26 455.993
78	(0 9 2)	19 695.475	124	(1 4 4)	23 521.137	170	(3 7 2)	26 473.194
79	(0 14 0)	19 725.491	125	(2 7 2)	23 541.071	171	(0 14 2)	26 541.770
80	(2 0 4)	19 757.078	126	(0 12 2)	23 586.875	172	(6 4 0)	26 561.608
81	(3 2 2)	19 883.532	127	(6 2 0)	23 815.333	173	(0 9 4)	26 616.364
82	(4 4 0)	20 055.970	128	(4 7 0)	23 844.389	174	(3 12 0)	26 667.025
83	(1 12 0)	20 126.492	129	(3 1 4)	23 905.143	175	(3 3 4)	26 712.413
84	(3 7 0)	20 377.122	130	(3 10 0)	23 952.473	176	(6 0 2)	26 821.827
85	(0 4 4)	20 398.165	131	(7 0 0)	23 981.179	177	(1 12 2)	26 856.530
86	(5 2 0)	20 428.273	132	(3 5 2)	23 994.704	178	(7 2 0)	26 906.477
87	(4 0 2)	20 532.285	133	(2 3 4)	24 177.676	179	(2 5 4)	26 913.996
88	(1 7 2)	20 638.087	134	(0 2 6)	24 193.434	180	(0 4 6)	26 976.959
89	(1 2 4)	20 709.799	135	(1 10 2)	24 196.931	181	(5 7 0)	26 992.399
90	(2 10 0)	20 731.617	136	(1 0 6)	24 309.341	182	(2 10 2)	27 038.163
91	(6 0 0)	20 913.135	137	(0 7 4)	24 362.057	183	(1 2 6)	27 166.932
92	(0 10 2)	20 914.649	138	(0 17 0)	24 395.029	184	(8 0 0)	27 278.631
93	(2 5 2)	21 020.257	139	(5 5 0)	24 510.074	185	(1 7 4)	27 290.117
94	(2 1 4)	21 204.889	140	(2 8 2)	24 667.417	186	(3 0 6)	27 418.387
95	(0 15 0)	21 277.726	141	(1 15 0)	24 725.352	187	(4 10 0)	27 430.372
96	(0 0 6)	21 284.273	142	(5 1 2)	24 776.462	188	(4 5 2)	27 452.780
97	(3 3 2)	21 332.285	146	(1 5 4)	24 836.461	189	(1 17 0)	27 476.584
98	(4 5 0)	21 377.841	144	(2 13 0)	24 917.000	190	(4 1 4)	27 525.925
99	(3 8 0)	21 545.071	145	(4 3 2)	24 928.973	191	(3 8 2)	27 636.881
100	(1 13 0)	21 652.376	146	(0 13 2)	24 984.896	192	(0 0 8)	27 678.444
101	(0 5 4)	21 757.548	147	(2 0 6)	25 035.096	193	(0 10 4)	27 714.336
102	(1 8 2)	21 831.166	148	(4 8 0)	25 086.363	194	(0 0 0)	27 718.858
103	(5 3 0)	21 842.567	149	(6 3 0)	25 217.600	195	(5 3 2)	27 735.648
104	(4 1 2)	22 011.076	150	(3 6 2)	25 246.132	196	(6 5 0)	27 840.080
105	(2 11 0)	22 050.281	151	(3 11 0)	25 257.407	197	(2 2 6)	27 851.784
106	(1 3 4)	22 133.360	152	(3 2 4)	25 349.054	198	(0 0 0)	27 863.548
107	(0 11 2)	22 208.244	153	(7 1 0)	25 439.946	199	(2 15 0)	27 990.982
108	(2 6 2)	22 303.928	154	(1 11 2)	25 488.318	200	(3 4 4)	28 031.264

^a E_{JN}^{\ddagger} are the vibrational energy levels calculated using the modified Jensen PES.

DD interactions results in states that are more simply described by local modes. Local modes are noted as $[nm]^{\pm}b$, in which n and m denote the stretching quanta in each bond and b denotes the bending quanta. As the anharmonicity in the O–H bond stretches increases, the interbond coupling becomes weaker and the vibrational states make a transition from normal mode to local mode.^{33–36} If the zeroth-order picture is best described by normal modes, the low excited vibrational states would show strong coupling between the two local modes and clear separation of Darling–Dennison resonance pairs. As ν increases, however, the Darling–Dennison interaction becomes dominant over the interbond coupling, and the normal basis starts to mix strongly. In reality the vibrations of a given molecule will correspond to a compromise between the two limiting cases, which depends on the topological characteristics of the potential energy surfaces.

The vibrational energy levels of H₂O exhibit normal mode patterns at low vibrational excitation, local mode patterns at intermediate excitation, and nonseparable patterns for very highly excited states. As the stretching vibrations become more highly excited, the anharmonicity leading toward bond dissociation tends to dominate, and thus the local mode model becomes a more accurate description of the molecular motions. Further excitation causes the molecule to explore wider scope of configuration space much more freely, and this results in extensive mixing of all vibrational modes.

Simple model studies have illustrated the roles of anharmonicity in O–H bond stretching and the coupling between the two bonds in giving rise to normal or local mode characteristics in the energy level patterns.^{37,36,38} The interbond coupling of the local mode basis is directly related to the energy splitting of symmetric and antisymmetric normal mode states, and the larger the coupling between the bonds the more likely it becomes the normal mode pattern. The magnitude of the coupling was shown to be proportional to $\nu=n+m$, in which n and m denote the excitations in the two bond oscillators, respectively.^{33,36}

In terms of local mode basis, the anharmonicities in bond stretchings may also result in transition from local to normal modes. The anharmonicity constants are directly related to the interactions among the Darling–Dennison

resonance pairs of normal modes. The Darling–Dennison couplings have dependence on $\nu_1\nu_3$, in which ν_1 and ν_3 denote the stretching quanta in symmetric and antisymmetric states. Recently, semiclassical dynamics has been used by Kellman and Xiao³⁵ in conjunction with an algebraic Darling–Dennison Hamiltonian to classify the stretching states of H₂O. They first showed that with this Hamiltonian the “polyad number,” n_a+n_s is conserved, but that within a polyad the states varied between normal mode and local mode type depending on the coupling in the DD Hamiltonian and the polyad number. In Tables VIII and IX, we have presented energy splittings of normal mode degenerate pairs whose linear combinations would correspond to the “degenerate” local mode states.

Table VIII lists energy splittings, δE , as a function of stretching quanta $\nu=\nu_1+\nu_3$ for the $\nu_2=0$ states of the two PES's. δE is the difference between the energy level of an antisymmetric state and that of a symmetric state. According to the simple model study,^{33,36} the energy splitting should decrease as the interbond coupling becomes smaller with an increase in ν . This is clearly seen for $[\nu 1]^\pm 0$ local-mode pairs which correspond to linear combinations of (3,0,0)/(2,0,1) series. On the other hand, the splittings of $[\nu 0]^\pm 0$ local-mode pairs which correspond to (0,0, ν)/(1,0, $\nu-1$) normal mode states do not decrease with increasing ν , in contrast to the predictions of the simple

TABLE VII. Antisymmetric vibrational energy levels of H₂O calculated using the JN surface. Energies are given in cm⁻¹.

n	(ν_1, ν_2, ν_3)	$E_{JN}^{\delta a}$	n	(ν_1, ν_2, ν_3)	$E_{JN}^{\delta a}$	n	(ν_1, ν_2, ν_3)	$E_{JN}^{\delta a}$
37	(2 5 1)	17 903.163	71	(0 8 3)	22 111.389	105	(1 8 3)	25 178.831
38	(0 0 5)	17 954.946	72	(3 6 1)	22 310.159	106	(2 6 3)	25 247.851
39	(3 3 1)	18 260.957	73	(0 3 5)	22 340.821	107	(2 11 1)	25 264.390
40	(1 8 1)	18 310.147	74	(2 0 5)	22 476.044	108	(2 2 5)	25 340.591
41	(0 5 3)	18 370.804	75	(1 1 5)	22 526.050	109	(1 3 5)	25 362.566
42	(2 1 3)	18 404.834	76	(3 2 3)	22 607.406	110	(6 1 1)	25 503.460
43	(0 11 1)	18 713.289	77	(2 9 1)	22 693.738	111	(3 4 3)	25 556.647
44	(1 3 3)	18 764.207	78	(2 4 3)	22 778.282	112	(0 11 3)	25 589.743
45	(4 1 1)	18 996.401	79	(1 6 3)	22 837.776	113	(4 6 1)	25 769.964
46	(2 6 1)	19 188.869	80	(0 14 1)	23 077.240	114	(3 9 1)	25 890.737
47	(0 1 5)	19 449.279	81	(0 9 3)	23 190.458	115	(0 1 7)	25 970.309
48	(1 9 1)	19 468.525	82	(4 4 1)	23 247.448	116	(0 16 1)	26 064.072
49	(3 4 1)	19 667.215	83	(4 0 3)	23 386.165	117	(5 0 3)	26 094.428
50	(0 6 3)	19 697.971	84	(1 12 1)	23 436.583	118	(5 4 1)	26 169.392
51	(3 0 3)	19 757.318	85	(5 2 1)	23 485.043	119	(1 9 3)	26 286.404
52	(2 2 3)	19 884.278	86	(3 7 1)	23 549.110	120	(4 2 3)	26 343.727
53	(0 12 1)	20 126.335	87	(0 4 5)	23 734.752	121	(1 14 1)	26 373.568
54	(1 4 3)	20 165.599	88	(2 1 5)	23 894.713	122	(0 6 5)	26 407.137
55	(2 7 1)	20 416.144	89	(2 10 1)	23 922.581	123	(3 1 5)	26 457.257
56	(4 2 1)	20 449.612	90	(1 2 5)	23 956.438	124	(2 7 3)	26 488.247
57	(5 0 1)	20 542.215	91	(2 5 3)	23 993.497	125	(2 12 1)	26 647.347
58	(1 10 1)	20 722.825	92	(6 0 1)	24 048.232	126	(1 4 5)	26 697.662
59	(0 2 5)	20 910.656	93	(1 7 3)	24 055.476	127	(2 3 5)	26 725.381
60	(0 7 3)	20 948.157	94	(3 3 3)	24 181.226	128	(7 0 1)	26 864.243
61	(3 5 1)	21 025.820	95	(0 10 3)	24 348.582	129	(0 12 3)	26 883.094
62	(1 0 5)	21 052.005	96	(0 0 7)	24 523.189	130	(3 5 3)	26 910.126
63	(3 1 3)	21 205.830	97	(4 5 1)	24 553.864	131	(6 2 1)	26 949.846
64	(2 3 3)	21 338.430	98	(0 15 1)	24 573.589	132	(3 10 1)	27 003.018
65	(1 5 3)	21 498.838	99	(3 8 1)	24 699.001	133	(4 7 1)	27 081.029
66	(2 8 1)	21 566.515	100	(4 1 3)	24 798.732	134	(0 2 7)	27 373.767
67	(0 13 1)	21 622.958	101	(1 13 1)	24 909.753	135	(6 0 3)	27 418.072
68	(4 3 1)	21 866.518	102	(5 3 1)	24 926.881	136	(5 5 1)	27 433.300
69	(5 1 1)	22 022.667	103	(3 0 5)	25 035.096			
70	(1 11 1)	22 041.817	104	(0 5 5)	25 088.326			

^a E_{JN}^{δ} are the vibrational energy levels calculated using the modified Jensen PES.

model. Since the Darling–Dennison coupling is strongly related to the anharmonicity of the bond stretching, zero excitation in one of the bonds is enough to inhibit the mixing of ν_1 and ν_3 .

Figure 2 is an energy diagram for $\nu = \nu_1 + \nu_3 = 2, 3, 4, 5, \text{ and } 6$. It illustrates the effect of the Darling–Dennison interactions on mixing of normal mode states, which would result in local modes in the limit of maximum mixing. In this figure, the zero of energy is set to the lowest-energy level among states of the same ν . As ν increases, a coupling between $(\nu_1, 0, \nu_3)$ and $(\nu_1 \pm 2, 0, \nu_3 \mp 2)$ becomes larger. For $\nu = 3$, the $(3, 0, 0)$ and $(1, 0, 2)$ states are strongly coupled such that it is hard to distinguish between the two states simply by counting the number of nodes in each mode. Furthermore, the order of energy levels for $(4, 0, 0)$ and $(2, 0, 2)$ states are switched from that of perfect normal modes. The arrows in the figure show splittings of Darling–Dennison resonance pairs. Larger Darling–Dennison interaction signifies smaller interbond coupling, which is typical of good local mode states.

Using our wave functions we have also evaluated the expectation values of R^2 and r^2 , from which the relative lengths of the two bonds are estimated. Namely,

$$X_1 = \frac{1}{\sqrt{2}} [(\langle R^2 \rangle)^{1/2} + (\langle r^2 \rangle)^{1/2}],$$

$$X_2 = \frac{1}{\sqrt{2}} [(\langle R^2 \rangle)^{1/2} - (\langle r^2 \rangle)^{1/2}].$$

Although X_1 and X_2 are not the expectation values of the individual bond lengths, the relative magnitude of X_1 and X_2 still give useful information regarding the assignments of local mode states among all states of the same ν . This is illustrated in Table X which contains X_1 and X_2 values for $\nu = 3$ and 5, which form relatively good local mode pairs. Schematic energy correlation diagrams of the normal and local mode limits are presented for $\nu = 3$ and 5 in Fig. 3. The center column of the figure corresponds to the calculated energy levels of the states that belong to the indicated normal mode assignments. The magnitudes of DD interactions vary for different normal mode pairs, which result in energy level patterns of the true states being much more complicated than that expected of simple models.³⁶

The polyad states with the most local mode character are the $(\nu_1 + 1 \nu_2 0)$ and $(\nu_1 \nu_2 1)$ pairs.³⁵ The effects of the bending mode, ν_2 , on the degeneracy of these local mode pairs is shown in Table IX for $\nu = \nu_1 + \nu_3 = 1, 3, \text{ and } 5$. These “local mode” energy splittings are plotted against the bending quanta in Fig. 4. Regardless of the fact that the average splittings for the three sets of ν states are quite different, their general pattern uniformly reflects an increase in the splitting as the energy in the bending coordinate approaches the barrier to the H–O–H linear configuration. The abrupt breaks in the plot, especially for the $\nu = 1$ plot, are the result of Fermi resonances for the particular states. Beyond the barrier to linearization, the bending motion gradually becomes a free rotor which would inhibit the kinetic coupling between the bonds. The de-

TABLE VIII. Local mode (n, m) ^a degeneracies as a function of stretching quanta for $\nu_2 = 0$ levels of H₂O, in cm⁻¹.

n	m	E_{JN}	ΔE^b	δE^c	E_{CH}	ΔE	δE
0	1	3656.49	3656.49	99.45	3656.32	3656.32	99.92
	2	7444.95	3788.46	-194.00	7442.63	3786.31	-193.82
	3	10 869.33	3424.38	164.79	10 856.92	3414.29	172.63
	4	14 541.33	3672.00	-219.82	14 531.71	3674.79	-230.43
	5	17 754.54	3213.21	200.41	17 717.69	3185.98	222.45
	6	21 284.28	3529.74	-232.27	21 260.63	3542.94	-259.55
	7	24 309.38	3025.10	213.86	24 233.57	2972.94	255.82
	8	27 678.72	3369.34	-226.93	27 496.79	3263.22	
1	0	3656.49	3656.49	99.45	3656.32	3656.32	99.92
	1	7202.67	3546.18		7204.35	3548.03	
	2	10 602.77	0602.77	12.83	10 608.34	3404.01	8.41
	3	13 829.73	3226.95	2.32	13 840.44	3232.09	0.61
	4	16 899.51	3069.78	0.07	16 915.21	3074.78	-0.31
	5	19 757.09	2857.58	0.24	19 786.30	2871.09	-0.09
	6	22 476.99	2719.90	-0.91	22 536.85	2750.54	-0.02
	7	25 035.21	2558.22	-0.01	25 131.12	2594.28	0.02
8	27 418.70	2383.49	-0.36	27 569.32	2438.20	0.82	
2	0	7444.95	3788.46	-194.00	7442.63		-193.82
	1	10 602.77	3157.82	12.83	10 608.34	3165.71	8.41
	2	14 223.50	3620.73		14 210.38	3602.04	
	3	17 460.86	3237.36	36.17	17 451.86	3241.48	22.97
	4	20 532.29	3071.43	9.93	20 522.86	3070.99	0.78
	5	23 380.89	2848.60	5.31	23 369.07	2846.21	-0.09
	6	26 097.47	2716.58	-2.89	26 137.27	2768.20	-2.35

^a (n, m) denotes the local mode representation for the stretching quanta of the two equivalent O–H bonds.

^b $\Delta E = E(n, m) - E(n, m - 1)$.

^c δE represents the local mode degeneracy and is the difference in energies of $(\nu_1 - 1, \nu_3 + 1)$ and (ν_1, ν_3) normal mode states. Here $\nu_1 + \nu_3 = n + m$.

TABLE IX. Local mode degeneracies as a function of ν_2 , bending quanta, for $\nu_1 + \nu_3 = 1, 3,$ and 5 of H_2O , in cm^{-1} .

ν	ν_2	E_{JN}	ΔE^a	δE^b	E_{CH}	ΔE	δE
1	0	3656.485		99.45	3656.321		99.92
	1	5234.285	1577.800	97.78	5234.458	1578.137	98.08
	2	6775.021	1540.736	98.45	6771.972	1537.514	100.61
	3	8273.243	1498.222	102.41	8266.479	1494.507	106.85
	4	9719.763	1446.520	112.84	9711.738	1445.259	117.68
	5	11 082.283	1362.520	152.94	11 087.290	1375.552	144.81
	6	12 504.089	1421.806	62.98	12 458.406	1371.116	107.40
	7	13 604.841	1100.752	194.41	13 625.417	1167.011	175.93
	8	14 778.301	1173.460	154.44	14 760.300	1134.883	171.76
	9	16 023.707	1245.406	84.52	15 948.181	1187.881	126.51
	10	17 312.440	1288.733	62.41	17 207.477	1259.296	116.45
	11	18 684.665	1372.225	28.62	18 561.372	1353.895	109.97
	12	20 126.492	1441.827	-0.16	19 994.520	1433.148	95.95
	13	21 652.376	1525.884	-29.42	21 476.177	1481.657	71.64
	14	23 168.743	1516.367	-91.50	22 863.550	1387.373	167.86
	15	24 725.352	1556.609	-151.76	24 312.492	1448.942	177.07
	16	26 233.960	1508.608	-169.89			
	17	27 718.868	1484.908	-169.99			
18	29 364.827	1645.959					
3	0	10 602.774		12.83	10 608.342		8.41
	1	12 144.462	1541.688	12.07	12 147.001	1538.658	6.92
	2	13 647.746	1503.284	10.98	13 641.528	1494.527	6.64
	3	15 109.671	1461.925	12.92	15 097.335	1455.807	7.56
	4	16 525.427	1415.756	15.76	16 511.603	1414.268	9.74
	5	17 877.874	1352.447	25.29	17 877.297	1365.694	14.21
	6	19 148.224	1270.350	40.64	19 180.484	1303.551	23.81
	7	20 377.122	1228.898	39.02	20 418.113	1237.265	30.11
	8	21 545.071	1167.949	21.44	21 562.952	1144.839	35.03
	9	22 743.593	1198.520	-49.85	22 608.596	1045.644	47.75
	10	24 196.933	1453.340	-274.34	23 745.501	1136.905	23.88
	11	25 488.321	1291.388	-223.92	24 976.182	1230.681	9.53
	12	26 856.549	1368.228	-209.20	26 291.103	1314.921	3.30
	13	28 160.137	1303.588	-318.27	27 643.818	1352.715	
14	29 364.735	1204.598		29 056.196	1412.378		
5	0	17 460.859		36.17	17 451.862		22.97
	1	18 958.419	1497.561	37.98	18 938.830	1486.968	22.19
	2	20 428.273	1469.854	21.34	20 386.582	1447.752	12.87
	3	21 842.567	1414.294	23.95	21 793.447	1406.865	14.32
	4	23 210.006	1367.439	37.44	23 163.229	1369.782	14.11
	5	24 510.074	1300.068	43.79	24 492.690	1329.461	22.35
	6	25 729.910	1219.836	40.05	25 780.665	1287.975	21.59
	7	26 992.399	1262.489	88.63	26 999.954	1219.289	33.42
	8	28 101.247	1108.848	71.85	28 148.730	1148.776	39.03
9	29 310.111	1208.864					

^a $\Delta E = E(n, m) - E(n, m - 1)$.

^b δE represents the local mode degeneracy and is the difference in energies of $(\nu_1 - 1, \nu_2, \nu_3 + 1)$ and (ν_1, ν_2, ν_3) normal mode states. Here, $\nu_1 + \nu_3 = n + m = 1, 3,$ and 5 .

crease in energy splittings between the local mode pairs is observed for intermediate levels. For very highly excited bending states, the extensive mixing between ν_1 and ν_2 interrupts the local mode degeneracies. At very high en-

ergy all vibrational degrees of freedom are strongly coupled, and neither the normal modes nor the local modes are a good description for the molecular vibrations.

Evidence of a clear transition from normal mode to

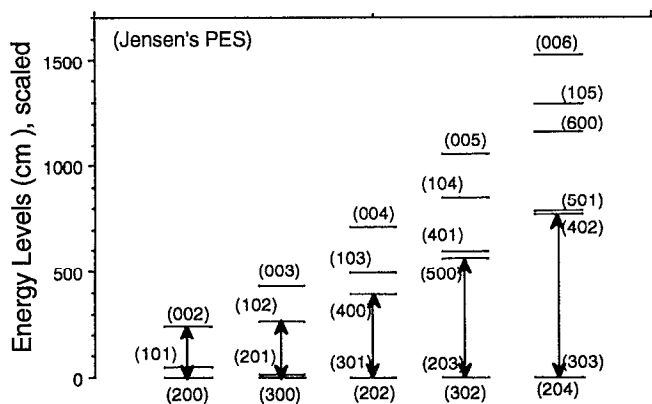


FIG. 2. The energy diagram of $\nu \equiv \nu_1 + \nu_3 = 2, 3, 4, 5,$ and 6 states (with $\nu_2 = 0$), illustrates the effects of the Darling-Dennison (DD) interactions. As ν increases, the DD interaction results in a stronger mixing of normal mode states and gives rise to states that are better represented by local mode descriptions. The zeros of energies in the diagram are set to the lowest energy level for the given ν .

local mode is shown in Fig. 5. Plotted in Fig. 5(a) are the energy spacings for progressions of $(\nu, 0, 0)$, $(\nu - 2, 0, 2)$, and $(\nu - 4, 0, 4)$ stretching states as a function of ν . For states which are well represented in terms of normal modes, the energy spacings should gradually decrease with ν . However, if the states are strongly coupled due to resonances rather irregular patterns may be expected which is clearly the case for $(\nu, 0, 0)$ progression. Likewise, Fig. 5(b) presents the energy spacings for progressions of $[n0]^+0$, $[n-1 1]^+0$, and $[n-2 2]^+0$ local mode states. For the $m=1$ progression, a gradual decrease in energy spacings reveals a simple anharmonicity in the local mode coordinate for those states. This results from a strong DD interaction between the corresponding normal mode pair.

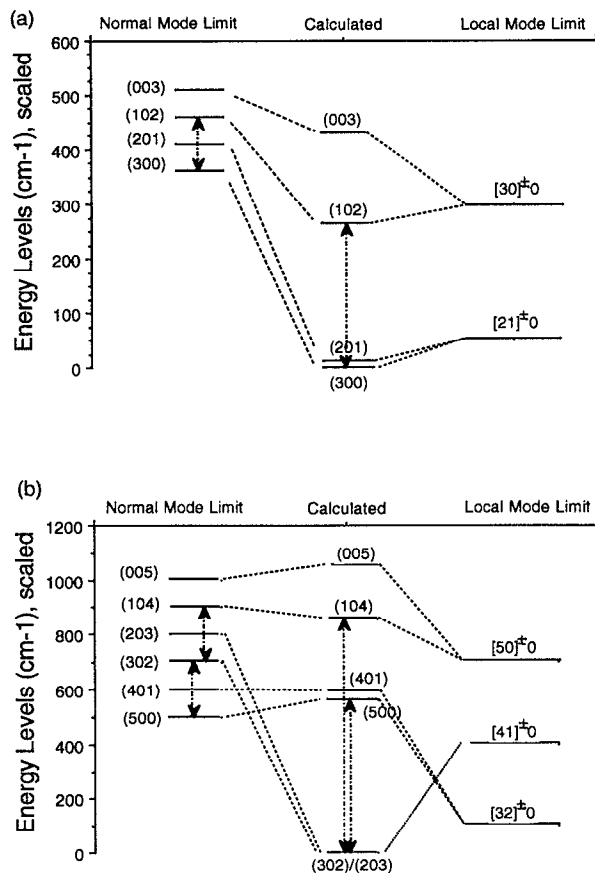


FIG. 3. Schematic energy correlation diagrams of the normal and local mode limits for $\nu=3$ and 5 . The center column is the calculated energy levels, assigned according to the normal mode descriptions. As a result of the unequal magnitudes of DD interactions for different normal mode pairs, the correlations between the two limiting representations are different from what is expected from a simple model. The zeros of energies are set to the lowest energy levels of the calculated values for the given ν states.

TABLE X. Relative O-H bond lengths, X_1 and X_2 , evaluated from $\langle R^2 \rangle$ and $\langle r^2 \rangle$ for $\nu=3$ and 5 states of $\nu_2=0$.

(ν_1, ν_3)	Jensen			Carter and Handy		
	E_{JN} (cm^{-1})	X_1 (\AA)	X_2 (\AA)	E_{CH} (cm^{-1})	X_1 (\AA)	X_2 (\AA)
(3, 0)	10 602.774	1.10	0.92	10 608.343	1.10	0.92
(2, 1)	10 615.601	0.91	1.11	10 616.752	0.91	1.11
(1, 2)	10 869.326	1.10	0.92	10 856.923	1.10	0.92
(0, 3)	11 034.111	0.88	1.13	11 029.553	0.88	1.13
(3, 2)	16 899.508	1.18	0.91	16 915.214	1.19	0.91
(2, 3)	16 899.580	0.91	1.18	16 914.907	0.91	1.19
(5, 0)	17 460.858	1.15	0.94	17 451.862	1.15	0.95
(4, 1)	17 497.030	0.92	1.17	17 474.828	0.92	1.17
(1, 4)	17 754.533	1.17	0.92	17 717.691	1.17	0.92
(0, 5)	17 954.946	0.88	1.19	17 940.137	0.92	1.17

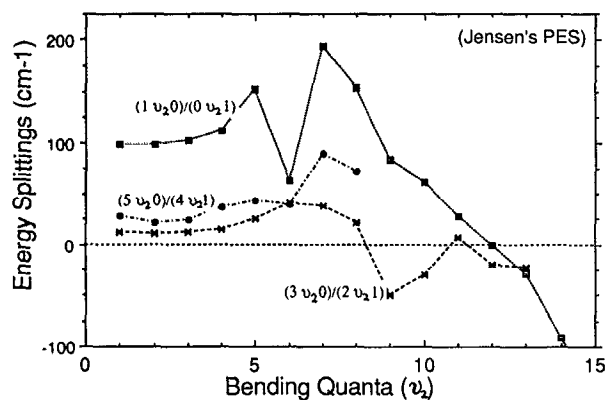


FIG. 4. For three different classes of $(\nu_1\nu_3)$ states, the energy splittings of local-mode pairs are plotted as a function of bending quanta, ν_2 . The plot of $(1\nu_2 0)/(0\nu_2 1)$ states shows a smooth increase in energy splittings with an abrupt discontinuity at $\nu_2=6$; the energy splitting, then, starts to decrease monotonically from $\nu_2=7$.

C. Separability of normal modes

The presence of resonances or local mode degeneracies can most easily be demonstrated in terms of separabilities of vibrational modes. States that have Fermi resonances should exhibit coupled stretching and bending modes, whereas the Darling–Dennison interaction will result in mixing of symmetric and antisymmetric stretching coordinates. The separability of vibrational modes can be systematically evaluated using the natural orbital expansion (NE) analysis of the wave functions.^{39–41} Since the symmetrized Radau coordinates exhibit close resemblance to normal modes, we have analyzed the separabilities of motions in (R, θ, r) which are assumed to imply the separabilities of $(\nu_1\nu_2\nu_3)$ normal modes. A detailed description of NE analysis is given in Appendix B.

The natural expansion analysis for a three-dimensional system involves re-expanding a wave function in terms of a direct product basis consisting of functions of one coordinate times functions of the other two coordinates. Thus, for systems involving three modes, separability of each mode from the remaining two is evaluated. The NE analysis gives the most rapidly convergent set of basis function of this form for each state analyzed. In NE analysis, the mode mixing is quantified in terms of the population probability coefficients, $\{d_q^2\}$, of the dominant configurations. As a measure, we define the “entropy of mixing,” S , as the following for each vibrational state and each coordinate:

$$S = \sum_q -d_q^2 \ln d_q^2 \quad (20)$$

Therefore, if there exists only one dominant configuration, then $d_1^2=1$, giving $S=0$. This will correspond to a case in which the coordinate is perfectly separated from the other two.

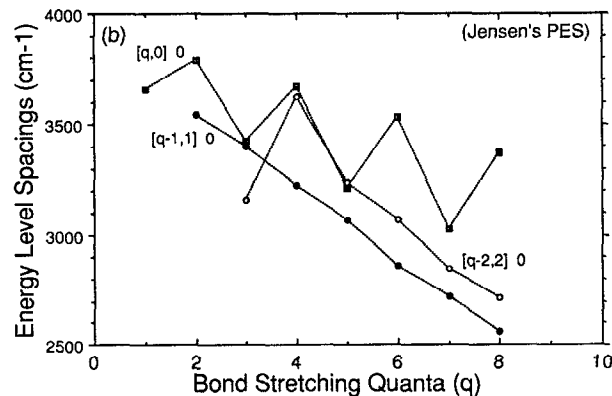
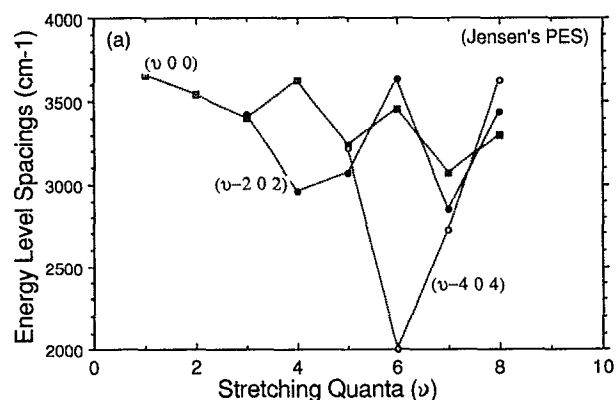


FIG. 5. (a) The three plots are the energy level spacings, ΔE , of symmetric stretching progressions for $\nu_3=0, 2$, and 4 states, respectively, shown as a function of ν . Each plot is indicated by its normal mode assignment, the first point corresponds to the energy difference between the $(10\nu_3)$ and $(00\nu_3)$ levels. The smooth decreases in ΔE due to anharmonicities in the symmetric stretch mode are only evident for low ν states. As ν increases, the normal mode description is not suitable. (b) The three plots are the energy-level spacings, ΔE , of progressions in a single O–H bond for $m=0, 1$, and 2 states, respectively, shown as a function of total bond stretching quanta, $\nu \equiv n+m$. Local mode assignment, $[n, m]^+0$, is given for each plot in which the first point corresponds to the energy difference between the $[1, m]^+0$ and $[0, m]^+0$ levels. For the $m=0$ progression, the local mode description is not suitable even for high ν states. On the contrary, a simple anharmonicity in the local mode coordinate is seen in the $[n, 1]^+0$ progression.

The effect of mode mixings on the local mode degeneracies is presented in Fig. 6 in terms of the entropies of the mode separabilities. Plotted in Figs. 6(a) and 6(b) are $[n0]^\pm 0$ and $[n1]^\pm 0$ local mode pairs, respectively. Solid lines indicate the symmetric states, and dotted lines are used for the antisymmetric states. Three different symbols denote the separabilities of R from (θ, r) : \circ , θ from (R, r) : \bullet , and r from (R, θ) : \blacksquare , respectively. Figure 6(a) and 6(b) clearly exhibit different patterns. The entropies of mixing for $[n1]^\pm 0$ pairs demonstrate close similarity in characteristics of the symmetric and antisymmetric vibrational states and thus represent much better local mode degeneracies. In Fig. 6(b), as n is increased Darling–Dennison interactions become larger which result in strong mixing of

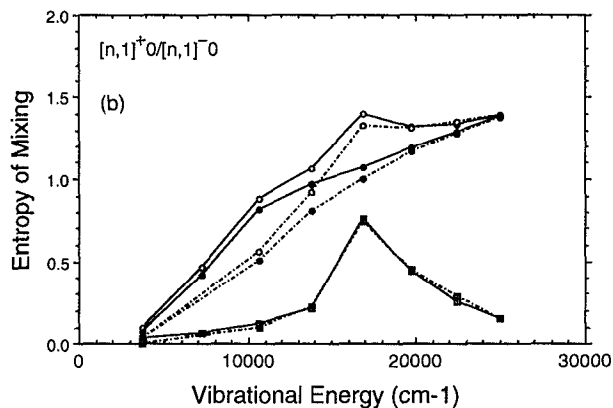
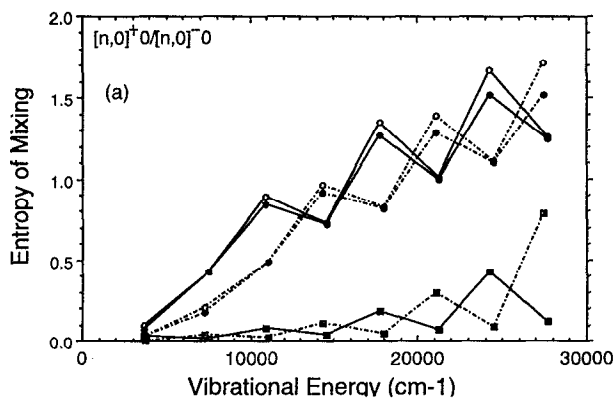


FIG. 6. (a) The entropies of mixings are plotted for local mode pairs, $[n,0]^{\pm 0}$, for n ranging from 0 to 7, as a function of the vibrational energy levels. The solid lines and the dot-dashed lines specify the + and - linear combinations of the local mode states, respectively. Different symbols are used to denote the mixings of different vibrational coordinates, $R/(\theta,r)[\]$, $\theta/(R,r)[\]$, and $r/(R,\theta)[\]$, respectively. (b) The entropies of mixings are plotted for local mode pairs, $[n,1]^{\pm 0}$; otherwise, the same as (a).

R and r to form local mode pairs. The entropy of mixing for the bend is the largest at $n=5$, and the mixing of θ with the stretching coordinates diminishes as the local mode degeneracies improve.

Figure 6(a), however, exhibits a very different pattern. The plots clearly indicate that the $[n,0]^{\pm 0}$ local mode states do not constitute good degenerate pairs. Even though mixing of R and r coordinates predominates as was in the case for $[n,1]^{\pm 0}$ states, the patterns of symmetric and antisymmetric states do not correlate, and therefore the mixing does not correspond to formation of local mode pairs. In addition, mixing of the bending coordinate with the stretches overall increases with ν .

Using the same symbols, Figs. 7(a) and 7(b) show the entropies of mixing for $(\nu_1,00)$ and $(00\nu_3)$ normal-mode states, respectively. ν_1 and ν_3 range from 1 to 8. The patterns of the separability of θ from (R,r) are quite different between the two figures. As the excitation in ν_1 increases,

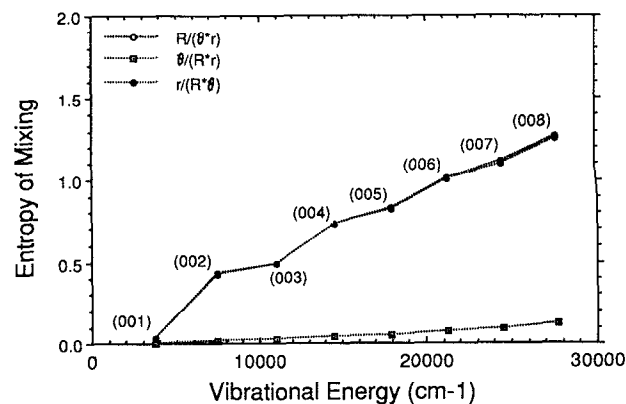
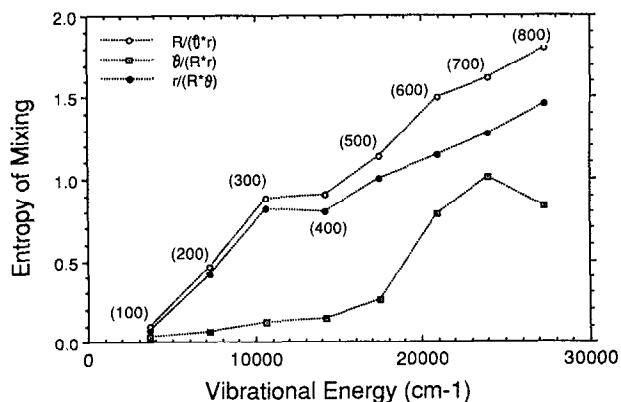


FIG. 7. The entropies of mixings are plotted as a function of vibrational energy levels for $(\nu_1,00)$ and $(00\nu_3)$ states. As ν_1 increases, mixing of the R and θ coordinates becomes stronger, diminishing the mixing of R and r . The θ coordinate is well separable even for highly excited ν_3 states.

so does the coupling of the bending with the stretches. On the contrary, the bends are quite separable from the stretching coordinates even for highly excited ν_3 states.

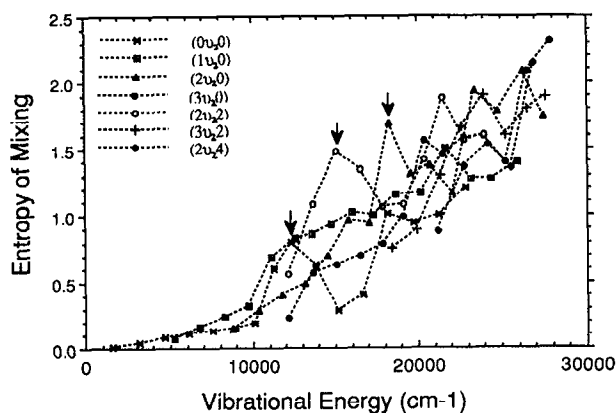


FIG. 8. An overlap of the entropies of mixing of the θ coordinate is presented for various sets of states as a function of energy levels. Each plot corresponds to the θ coordinate a specific (ν_1,ν_3) state as ν_2 progresses. $(0\nu_2,0)$:■; $(1\nu_2,0)$:□; $(2\nu_2,0)$:▲; $(3\nu_2,0)$:●; $(2\nu_2,2)$:○; $(3\nu_2,2)$:+; and $(2\nu_2,4)$:◆. The arrows indicate states whose entropies of mixing are enhanced by accidental resonances.

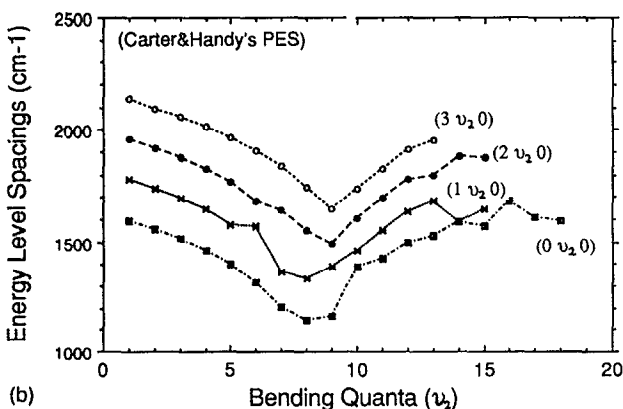
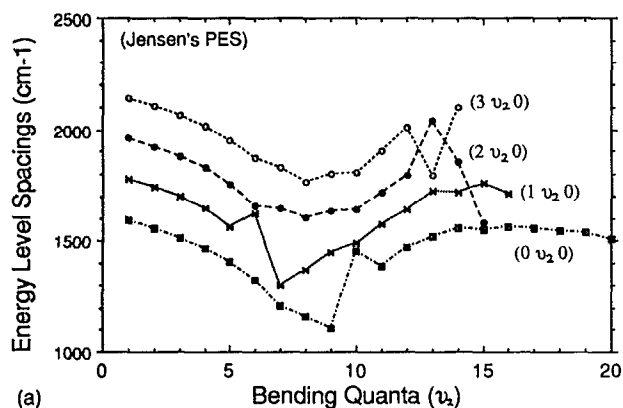


FIG. 9. For $\nu_1=0, 1, 2,$ and 3 (and $\nu_3=0$), the energy level spacings, ΔE , between ν_2 and ν_2-1 states are plotted as a function of ν_2 . (a) and (b) correspond to the energies calculated from the modified JN and CH PES's, respectively. Overall, for both PES's the level spacings monotonically decrease up to $\nu_2=9$, beyond which increases in spacings are evident. An accidental resonance, such as (090) and (160) states, clearly disrupts the smooth pattern of energy levels. Sharper changes of the levels spacings are shown for higher ν_1 states of the CH PES.

This, in turn, results in stronger coupling between the symmetric and antisymmetric stretches for excitation in ν_3 .

Finally, the separability of θ for bending progressions of different stretching states are plotted as a function of their energy levels in Fig. 8. The arrows indicate states whose entropies of mixing are enhanced due to Fermi resonances. The overall pattern of the entropies for the mixing of θ coordinate is increasing exponentially.

D. Fermi resonances

In H_2O , the fundamental frequencies of symmetric stretching, ν_1 , and bending, ν_2 , are 3657 cm^{-1} and 1595 cm^{-1} which are near to a 1:2 resonance. Because of the relatively low energy barrier to linearization for H-O-H configurations, which is $\sim 12\,500 \text{ cm}^{-1}$ for the O-H bond length near its equilibrium, the PES is extremely anharmonic in θ , and the energy spacings decrease to ~ 1100

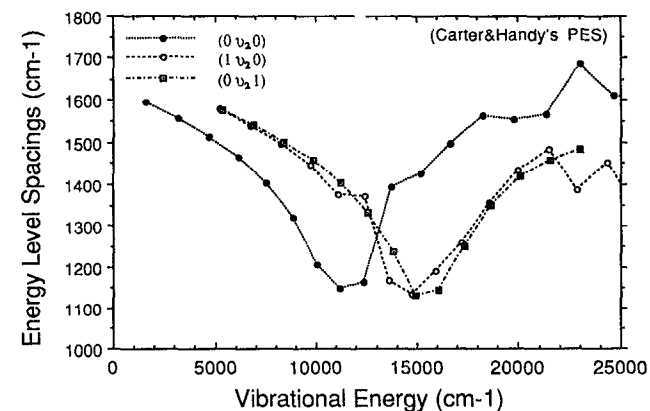
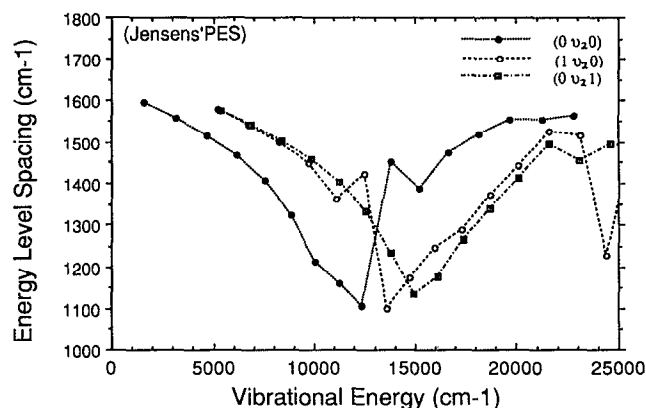


FIG. 10. The energy level spacings of bending progressions, $0 \leq \nu_2 \leq 16$, are plotted for $(0\nu_2 0)$:●; $(1\nu_2 0)$:○; and $(0\nu_2 1)$:□ states from JN and CH PES's.

cm^{-1} between $\nu_2=8$ and 9 . Around this energy level, the resonance between the stretch and the bend is closer to 1:3. As the excitation in the bend increases even further above the energy of the barrier, the spacings of bending energy levels start to increase, corresponding to a more free rotor-type motion as an H atom orbits around the center of mass of O-H. These large changes in the bend frequency cause complicated resonance patterns throughout the energy levels.

The spacing of energy levels, ΔE , of bending progressions for $(\nu_1\nu_2 0)$ normal mode states with $0 \leq \nu_1 \leq 3$ are plotted as a function of ν_2 in Fig. 9. Monotonic decreases in energy spacings are clearly evident up to $\nu_2=9$ for most stretching states. For $\nu_2 > 9$ ΔE gradually increases. A comparison between the plots from JN's and CH's surface shows that the general patterns of the δE curves are quite similar. The main difference is in the smoother increase of ΔE about $\nu_2=9$ for higher excited stretching states from the CH surface. The irregularities in the pattern are more distinct for the excited ν_2 states of JN's surface, which imply more extensive mixing of the mode. The abrupt

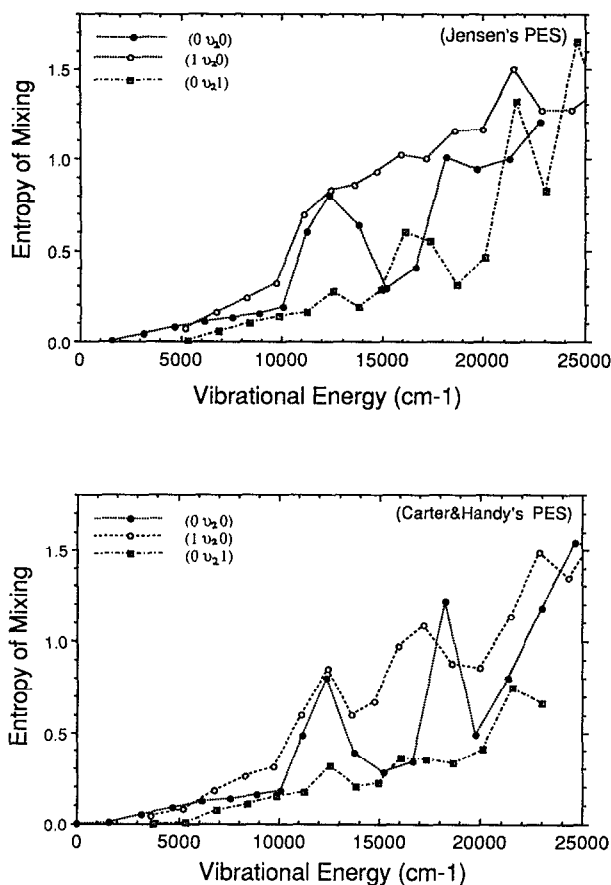


FIG. 11. The entropies of mixing of the θ coordinate are plotted for the bending ($0 < \nu_2 < 16$) progressions of $(0\nu_20)$, $(1\nu_20)$, and $(0\nu_21)$ states for JN and CH PES's.

breaks in the ΔE curves occur most evidently at (090) and (160) for both surfaces.

ΔE 's of the bending progressions of $(0\nu_20)$, $(1\nu_20)$, and $(0\nu_21)$ are plotted in Fig. 10 as a function of total vibrational energy. In this figure, one can clearly see that the Fermi resonance between the (090) and (160) states causes a strong interaction, creating an irregular spacing in their energies. The $(0\nu_21)$ plot does not reveal any unusual pattern due to resonances.

For the same set of states as in Fig. 10, the entropic measures for the separabilities of the bending, θ , coordinate from the stretching coordinates (R, r), are plotted in Fig. 11. Abrupt increases in the entropy of the θ mixing is evident for the (090) and (160) states. This is due to the 1:3 Fermi resonance between the stretch and the bend. The mixing becomes more intense as the vibrational energy increases. For $(0\nu_21)$ states, the mixing of a bending mode occurs at much slower rate than the $(1\nu_20)$ states.

The plots of Fig. 12 are the entropic measures for the separabilities of all modes for $(\nu_1\nu_2\nu_3) = (0\nu_20)$, $(3\nu_20)$, and $(0\nu_23)$ states of the JN and CH surfaces. The three plots of each column illustrate quite specific effects. The $(0\nu_20)$ states show the effect of the Fermi resonance near

(090) but the antisymmetric stretch coordinate is well separated from (R, θ) . The $(3\nu_20)$ series starts with strong (R, r) coupling due to local modes, and then shows increasing (θ, R) mixing with ν_2 . Finally, the $(0\nu_23)$ sequence shows quite low mixing of all modes until an energy above $25\,000\text{ cm}^{-1}$ is attained. These sequences indicate that in H_2O (on the modified JN surface at least), the mode mixing is very specific and that some states remain quite separable to very high vibrational energies.

E. Statistical studies on the vibrational energy levels

The energy level spacing distribution has been considered as a positive test for the manifestation of classical chaos in quantal systems. In theory, the level spacing distribution of a quantal system gradually changes from a Poisson type to a Wigner type as the system becomes more fully "chaotic." Chaotic behavior of a classical system may be identified with extensive mixing among all the nuclear degrees of freedom. In general, this will lead quantum mechanically to level "repulsion" and a more uniform pattern of energy level spacings. Chaotic nodal structures of the wave functions are also considered as means of identifying "quantum chaos."

Earlier we discussed specific types of resonance effects that may result in coupling between vibrational states. Due to the complicated interactions among highly excited levels, we could only give the representative examples for different types of resonances. The statistical studies of energy level spacings including all energy levels, however, are simple to present and conceptually easy to interpret for the global characteristics of the molecular vibrational levels.

In Fig. 13 we plot the histogram of the locally average level spacing, $\Delta\epsilon_n$, where

$$\Delta\epsilon_n \equiv \epsilon_{n+1} - \epsilon_n \quad (21a)$$

$$= (2L+1) \frac{E_{n+1} - E_n}{E_b - E_a}, \quad (21b)$$

in which E_i denotes the i th energy level, and $2L+1$ the number of levels included in the local average, $b = n+L$, and $a = n-L$. We have evaluated the averaging for L ranging between 3 and 15. The statistical behavior stabilizes for $5 \leq L < 9$. We also checked for the effects of the bin size, δ , of the histogram on the distribution. For $\delta \leq 0.05$ the statistical distribution was not affected by it.

The histograms in Fig. 13 are evaluated for $L=5$ and $\delta=0.05$ for the two PES's. There are obvious differences between the two plots. The second moments of the distributions for the two surfaces are 1.4 and 1.7 for JN's and CH's, respectively. Thus, the CH surface produces a distribution much nearer the Poisson type ($\sigma=2.00$) which is characteristic of separable systems. For both surfaces, the statistical distributions show a slow decrease in the second moment as the studies include states of increasing energy. For both surfaces, the energy level spacing distributions were analyzed as the maximum energy level was incrementally increased from $20\,000$ to $37\,000\text{ cm}^{-1}$ above the zero-

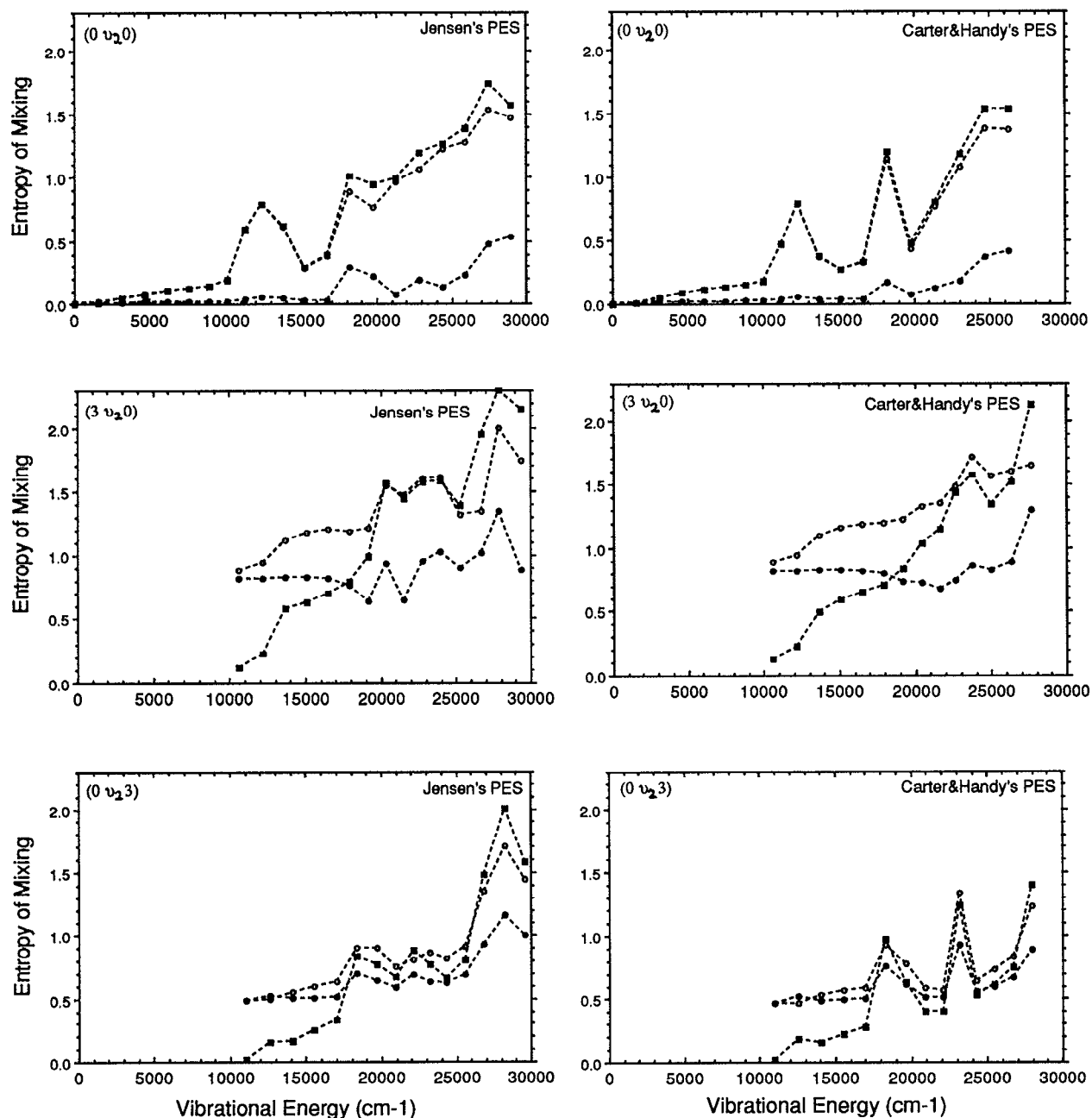


FIG. 12. Separabilities of the three vibrational modes are presented. The entropies of mixing for $R/(\theta*r)$: \circ ; $\theta/(R*r)$: \blacksquare ; and $r/(R*\theta)$: \bullet are overlapped for bending progressions of $(0, \nu_2, 0)$, $(3, \nu_2, 0)$, and $(0, \nu_2, 3)$ stretching states. The characteristics of states of the JN and CH PES's may be compared.

point energy. The second moments ranged from 1.53 to 1.45 for the JN surface, and ranged from 1.72 to 1.63 for the CH surface for symmetric vibrational states. The apparent patterns of distributions do not change much over a wide range of energy levels.

The entropic analysis of the natural orbital expansion analysis for all symmetric states is presented in Fig. 14. Although the mixing increases, as expected, with energy for all coordinate separations, both JN and CH surfaces

show interesting behavior with respect to the antisymmetric stretch separation. Note that a set of states remains almost completely separable ($S < 0.25$) up to over 20 000 cm^{-1} and a second set of states show only local mode mixing ($S \sim \ln 2 = 0.69$) up to comparable energy. These separable sets which are most pronounced for the antisymmetric stretch coordinate, r , persist to higher energy for the CH surface.

Finally, we may comment that H_2O is an interesting

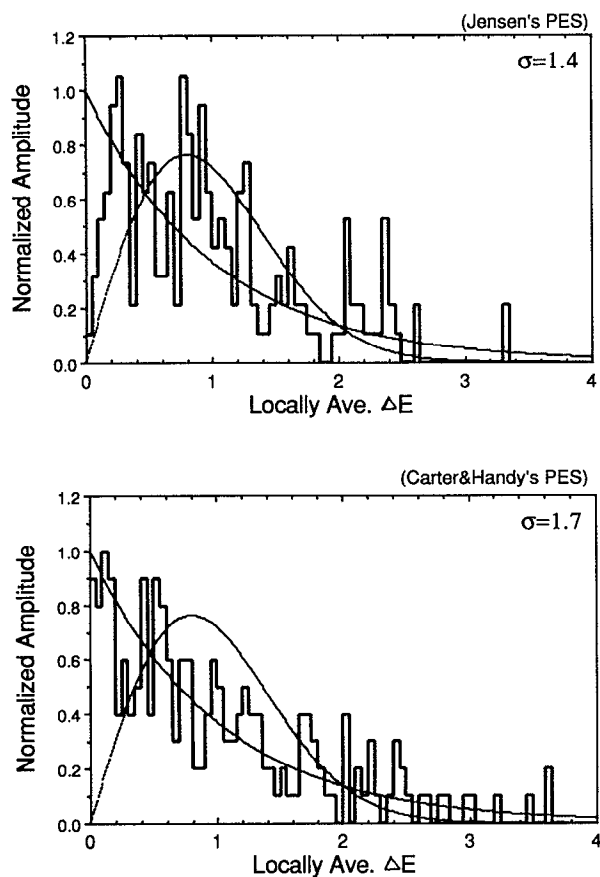


FIG. 13. Histograms of the locally averaged nearest-neighbor energy level spacing distributions for symmetric and antisymmetric vibrational states computed from the JN and CH PES's. The second moments σ of the histograms are given, and the Poisson and Wigner distributions are overlapped.

molecule, if very difficult one to make generalizations about. Although local modes do exist in a given energy regime, there is no distinct "local mode transition," and local and normal mode type states coexist in a reasonable energy range. Numerous specific interactions occur, but separability of some antisymmetric stretch states persists to very high energy. Finally, the energy level spacing distributions merely creep toward the Wigner distribution as the energy range increases.

In the near future we will present a summary of results for H_2O in rotational states up to $J \leq 15$, in which effects of rotation on mixing are examined.

V. CONCLUSION

We have examined the dynamical characteristics of vibrationally highly excited (floppy) H_2O using DVR. Since the nature of energy flow within polyatomic molecules is an important factor controlling chemical kinetics, such calculations are of interest to many different areas of chemical physics. Anomalous patterns of spectra frequently re-

sult from extensive mixing among zeroth-order modes. The DVR approach offers a powerful means of computing accurate energy levels in a wide energy range, while retaining a simple physical picture of the dynamics of molecules even in highly excited states.

H_2O has been one of the most widely studied molecule, both theoretically and experimentally. The rovibrational spectra of the highly excited stretching states with low bend excitations have revealed patterns of normal to local mode transitions as well as Fermi resonance interactions. Theoretically, reduced dimensional studies of classical dynamics have predicted transitions to chaos at highly excited vibrational states due to overlaps of various resonances. At the beginning of our study, we anticipated that we would be able to characterize the intriguing aspects of the intramolecular dynamics of the water molecule in some relatively straightforward fashion as a function of the vibrational energy. As indicated by the analyses above, however, different vibrational states of H_2O exhibit characteristics of different zero-order decompositions over a wide range of energy.

Although local modes do exist over a wide energy range, there are, for each polyad, as pointed out by Kellman and Xiou,³⁵ states which have dominant normal mode character. In addition, the adequacy of the normal mode/local mode characterization is rather strongly dependent on the bending quantum number, ν_2 . The degree of local-mode degeneracy is found to be strongly dependent on the extent of mixing between ν_1 and ν_2 (or ν_3 and ν_2) rather than on the vibrational energy alone. In particular, the natural orbital analysis and the degeneracies (or lack thereof) between symmetric and antisymmetric states indicate that local and normal mode type states coexist in a reasonable energy range. One has, in fact, "interpenetrating lattices" of local mode, normal mode, and very mixed type states above about $15\,000\text{ cm}^{-1}$ for both the Carter-Handy surface and the Jensen surface. The basic characteristics of the normal to local mode transitions are the same for the two different PES's that are analyzed.

The entropies of mixing, evaluated from the natural orbital analysis, are a measure of vibrational mode couplings. These measures depend only on the coordinate system used (normal mode type), but not on the basis sets. The entropy is most sensitively dependent on the vibrational quanta in the ν_2 mode. Even though numerous specific interactions (spectroscopic perturbations such as Fermi resonances and Darling-Dennison interactions) occur throughout the energy range, the separability of some antisymmetric stretch states persists to very high energy. These states undoubtedly correspond to low bend states.

Finally, a statistical analysis of the energy level spacing distributions shows merely a mild inclination toward the characteristics of the Wigner distribution as the energy range increases. However, it does reveal surprisingly different dynamical characteristics for the two PES's, with the Jensen surface exhibiting stronger chaotic tendencies as compared to the Carter-Handy surface.

In contrast to simple analytical model studies or reduced dimensional classical dynamics, our study has

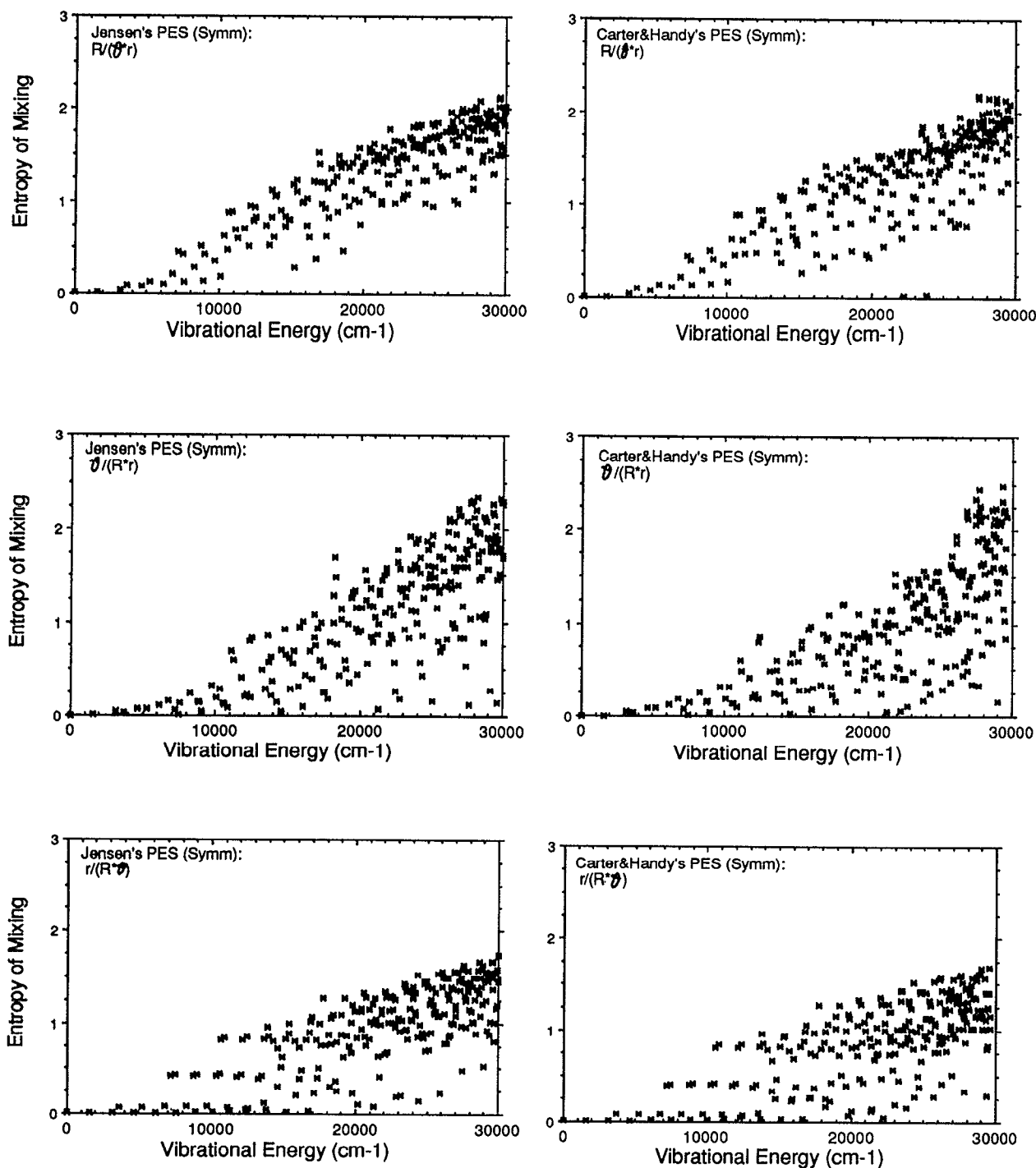


FIG. 14. The entropies of mixing for $R/(\theta^*r)$, $\theta/(R^*r)$, and $r/(R^*\theta)$ are presented for all symmetric states as a function of vibrational energy in separate plots.

shown that there is no clear energy dependence to local mode transition or the onset to chaotic behavior of energy levels. We have not been able to make any generalization as regards to the effect of overlapping resonances on the intramolecular dynamics.

ACKNOWLEDGMENTS

We gratefully acknowledge the support of this research by a grant from the National Science Foundation, No. NSF CHE-8806514.

APPENDIX A: BASIS FUNCTIONS

In this appendix we give the exact definitions of basis functions and DVR's which we use.⁴²

1. Chebyshev functions

A normalized Chebyshev (first kind) polynomial of order l is generally defined by

$$\mathcal{F}_l(q) = A_l \cos(l \arccos q), \quad (A1)$$

where $q \in [-1, 1]$. Defining $q = \cos \phi$, $\Delta R = R_f + R_i$ and scaling according to

$$\phi = \frac{(R - R_i)}{\Delta R} \cdot \pi \quad (\text{A2})$$

for $R \in [R_i, R_f]$, the Chebyshev basis functions (FBR) are given by

$$\mathcal{F}_l(R) = A_l \cdot \cos(l\phi), \quad (\text{A3})$$

where

$$A_l = \sqrt{(2 - \delta_{l0}) / (R_f - R_i)}. \quad (\text{A4})$$

The orthonormality condition is satisfied

$$\delta_{l'l} = \int_{R_i}^{R_f} \mathcal{F}_{l'}(R) \cdot \mathcal{F}_l(R) dR, \quad (\text{A5})$$

and the kinetic energy operator is diagonal in the Chebyshev basis:

$$\frac{\partial^2 \mathcal{F}_l(R)}{\partial R^2} = -R d_l \mathcal{F}_l(R) \quad (\text{A6})$$

for

$$R d_l = \left(\frac{\pi l}{\Delta R} \right)^2. \quad (\text{A7})$$

For an N_R function basis, the DVR-FBR transformation can be formed by diagonalization of the matrix representation of the coordinate R in the FBR.^{17,15,16} The eigenvalues are the Gauss-Chebyshev quadrature points, R_α , and the orthonormal transformation matrices can be written using the Gaussian weights ω_α as

$$t_{l\alpha} = \sqrt{\omega_\alpha} \cdot \mathcal{F}_l(R_\alpha), \quad (\text{A8})$$

where

$$R_\alpha = R_i + (\alpha - \frac{1}{2}) \cdot \delta R, \quad (\text{A9a})$$

$$\omega_\alpha = \delta R, \quad (\text{A9b})$$

$$\delta R = (R_f - R_i) / N_R. \quad (\text{A9c})$$

The DVR basis functions are

$$\Gamma_\alpha(R) = \sum_l^{N_R} t_{l\alpha} \mathcal{F}_l(R). \quad (\text{A10})$$

The approximations that coordinate functions are diagonal in the DVR is equivalent to evaluation of the DVR matrix elements by the N_R -point Gaussian quadrature. The relation is shown by evaluating a matrix element of a function, $\{\mathcal{F}_l(R)\}$, in the FBR:

$$\begin{aligned} \text{FBR} \mathbf{F}_{l'l} &\equiv \int_{R_i}^{R_f} \mathcal{F}_{l'}(R) \cdot f(R) \cdot \mathcal{F}_l(R) dR \\ &\simeq \sum_{\alpha=1}^{N_R} \omega_\alpha \cdot \mathcal{F}_{l'}(R_\alpha) \cdot f(R_\alpha) \cdot \mathcal{F}_l(R_\alpha) \\ &= \sum_{\alpha} t_{l'\alpha} \cdot f(R_\alpha) \cdot t_{l\alpha}. \end{aligned} \quad (\text{A11})$$

Therefore,

$$\text{FBR} \mathbf{F} \simeq \mathbf{t} \cdot \text{DVR} \mathbf{F} \cdot \mathbf{t}^T \quad (\text{A12})$$

and

$$\text{DVR} \mathbf{F}_{\alpha'\alpha} = f(R_\alpha) \cdot \delta_{\alpha'\alpha}. \quad (\text{A13})$$

Since the Gaussian quadrature is exact for the coordinate R , the orthogonal transformation matrices \mathbf{t} diagonalize the FBR matrix of R , $\text{FBR} \mathbf{R}$.

2. Harmonic functions

The harmonic oscillator functions can be defined by the self-adjoint form of the second-order differential equation for Hermite polynomials times the Gaussian weight function. The equation for the harmonic oscillator functions is

$$\frac{\partial^2 \mathcal{H}_j(q)}{\partial q^2} = -[(j + \frac{1}{2}) - q^2] \cdot \mathcal{H}_j(q). \quad (\text{A14})$$

The variable q of the function is appropriately scaled to $r, q = \zeta r$. The kinetic energy matrix element in the FBR is then

$$\mathbf{L}'_{j'j} \equiv \int_{-\infty}^{\infty} \mathcal{H}_{j'}(r) \cdot \frac{-\partial^2}{\partial r^2} \mathcal{H}_j(r) dr = {}^r d_j \cdot \delta_{j'j} - P_{j'j}, \quad (\text{A15})$$

where

$${}^r d_j = \xi^2 (j + \frac{1}{2}), \quad (\text{A16a})$$

$$P_{j'j} = \int_{-\infty}^{\infty} \mathcal{H}_{j'}(r) \cdot \xi^4 r^2 \cdot \mathcal{H}_j(r) dr \quad (\text{A16b})$$

for the orthonormal set of functions in r ,

$$\int_{-\infty}^{\infty} \mathcal{H}_{j'}(r) \cdot \mathcal{H}_j(r) dr = \delta_{j'j}. \quad (\text{A17})$$

Again, the DVR points and transformation can be obtained as eigenvalues and eigenvectors of the coordinate matrix, ζr ,

$$\text{FBR} \mathbf{r} \cdot \mathbf{t} = \mathbf{t} \cdot \text{DVR} \mathbf{r} (\text{diag}). \quad (\text{A18})$$

The DVR basis is

$$\Phi_\beta(r) = \sum_j^{N_r} t_{j\beta} \cdot \mathcal{H}_j(r). \quad (\text{A19})$$

For a basis of even or odd symmetry, the harmonic DVR basis is symmetrized:

$$({}^g) \Phi_\beta(r) = \frac{1}{\sqrt{2}} [\Phi_\beta(r) + (-1)^q \Phi_{\beta'}(r)], \quad (\text{A20})$$

where $q=0, 1$ for even or odd symmetry and $\beta' = N_r - \beta + 1$ for $\beta=1, 2, \dots, N_r/2$. From the definition of the transformation matrices in Eq. (8b), we see that

$$t'_{j\beta'} = \begin{cases} t_{j\beta} & \text{for } j=\text{even}, \\ (-1) t_{j\beta} & \text{for } j=\text{odd}. \end{cases} \quad (\text{A21})$$

Therefore the transformation from even (or odd) FBR basis functions to even (or odd) DVR functions can be formed as

$$\begin{aligned} \begin{pmatrix} S\Phi_\beta(r) \\ A\Phi_\beta(r) \end{pmatrix} &= \frac{1}{\sqrt{2}} \cdot \begin{pmatrix} 1 & 1 \\ 1 & -1 \end{pmatrix} \begin{pmatrix} \Phi_\beta(r) \\ \Phi_{\beta'}(r) \end{pmatrix} \\ &= \frac{1}{\sqrt{2}} \cdot \begin{pmatrix} 1 & 1 \\ 1 & -1 \end{pmatrix} \begin{pmatrix} \mathbf{t}_{j\beta}^e & \mathbf{t}_{j\beta}^o \\ \mathbf{t}_{j\beta'}^e & \mathbf{t}_{j\beta'}^o \end{pmatrix} \begin{pmatrix} \mathcal{H}_j^e(r) \\ \mathcal{H}_j^o(r) \end{pmatrix} \end{aligned} \quad (\text{A22})$$

$$= \sqrt{2} \cdot \begin{pmatrix} \mathbf{t}_{j\beta}^e & 0 \\ 0 & \mathbf{t}_{j\beta}^o \end{pmatrix} \begin{pmatrix} \mathcal{H}_j^e(r) \\ \mathcal{H}_j^o(r) \end{pmatrix}, \quad (\text{A23})$$

i.e. we have

$${}^{(g)}\Phi_\beta(r) = \sqrt{2} \sum_{j=(q)} \mathbf{t}_{j\beta} \mathcal{H}_j(r), \quad (\text{A24})$$

restricted to the functions $(q) = \text{even}$ or odd for $(g) = S$ or A , respectively.

Since the kinetic energy operator in r does not couple basis functions of different symmetries, the \mathbf{K}^r matrix evaluated in $\{{}^{(g)}\Phi_\beta\}$ will have a block-diagonal form separated by symmetry of the basis, which consists of elements determined by

$${}^{(g)}\mathbf{K}_{\beta'\beta}^r = \sum_{j'=(q)} \sum_{j=(q)} \mathbf{t}_{j'\beta'}^r \cdot \mathbf{L}_{j'j}^r \cdot \mathbf{t}_{j\beta}^r \quad (\text{A25a})$$

$$= \left[\sum_{j=(q)} \mathbf{t}_{j\beta'}^r \cdot {}^r d_j \cdot \mathbf{t}_{j\beta}^r \right] - \zeta^A r_\beta^2 \cdot \delta_{\beta'\beta} \quad (\text{A25b})$$

in which the orthogonality of the DVR basis functions has been applied. The ${}^{(g)}\mathbf{K}^r$ -matrix elements are summed over either even or odd manifolds of functions

3. Jacobi polynomials

The kinetic energy matrix in θ is evaluated using the Jacobi polynomials defined according to the self-adjoint form of the second-order differential equation,

$$\begin{aligned} \mathbf{L}_{i'i}^\theta &\equiv \int_0^\pi \mathcal{F}_{i'}^{(a,b)}(x) \cdot \left(-\frac{1}{\sin \theta} \frac{\partial}{\partial \theta} \sin \theta \frac{\partial}{\partial \theta} \right) \cdot \mathcal{F}_i^{(a,b)}(x) dx \\ &= {}^\theta d_i \cdot \delta_{i'i} + {}^\theta P_{i'i}, \end{aligned} \quad (\text{A26})$$

where

$${}^\theta d_i = i(i+a+b+1) + \frac{(a+b+ab)}{2} + \frac{(a^2+b^2)}{4}, \quad (\text{A27a})$$

$${}^\theta P_{i'i} = \int_0^\pi \mathcal{F}_{i'}^{(a,b)}(x) \cdot p(x) \cdot \mathcal{F}_i^{(a,b)}(x) dx, \quad (\text{A27b})$$

$$p(x) = - \left[\frac{a^2}{4 \sin^2(\theta/2)} + \frac{b^2}{4 \cos^2(\theta/2)} \right], \quad (\text{A27c})$$

and for which

$$\int_0^\pi \mathcal{F}_{i'}^{(a,b)}(x) \cdot \mathcal{F}_i^{(a,b)}(x) dx = \delta_{i'i} \quad (\text{A28})$$

defines the orthonormality of the functions. The parameters a and b may be chosen to optimize the basis for a given problem based on (i) cancellation, full or partial, of effective

potential singularities in Eq. (3), and (ii) satisfaction of appropriate boundary conditions at $\theta=0, \pi$.

The $1/\cos^2(\theta/2)$ term in the effective potential $p(x)$ can partially cancel out the same term in Eq. (3). If $b=k$, a complete cancellation would result. If $b=0$ and $k=0$, no singularity arises from $1/\cos^2(\theta/2)$. As mentioned earlier, however, for $k \neq 0$ but even, the parameter b of the polynomials must be zero in order to allow (correctly) amplitudes of wave functions at $\theta=\pi$, and the singularity is not fully eliminated. In our computation of $\{\varphi_q^{\text{vib}}\}$ for even k 's, $b=0$ is used for Jacobi polynomials. By setting $a \neq 0$, $\theta_\gamma > 0$, the effects of the singularity due to $1/\sin^2(\theta/2)$ is completely eliminated.

The unitary transformation of \mathbf{L}^θ to the DVR is obtained by diagonalization of $\cos \theta$ and yields the kinetic-energy operator in the DVR:

$$\mathbf{K}_{\gamma'\gamma}^\theta = \sum_{i',i} \mathbf{t}_{i'\gamma'}^\theta \cdot \mathbf{L}_{i'i}^\theta \cdot \mathbf{t}_{i\gamma}^\theta \quad (\text{A29a})$$

$$= \left[\sum_i \mathbf{t}_{i\gamma'}^\theta \cdot {}^\theta d_i \cdot \mathbf{t}_{i\gamma}^\theta \right] - p(x_\gamma) \cdot \delta_{\gamma'\gamma}, \quad (\text{A29b})$$

applying the orthogonality of the DVR basis functions.

According to Eq. (3), a first-order derivative in θ appears in $\delta_{k'k+1}$ block of Hamiltonian. We use the recurrence relation to evaluate it:

$$\begin{aligned} \frac{d}{d\theta} \mathcal{F}_i^{(a,b)}(x) &= -\sin \theta \frac{d}{dx} \mathcal{F}_i^{(a,b)}(x) \\ &= g^i(x) \cdot \mathcal{F}_i^{(a,b)}(x) + g^{i-1}(x) \cdot \mathcal{F}_{i-1}^{(a,b)}(x), \end{aligned} \quad (\text{A30})$$

where

$$\begin{aligned} g^i(x) &= \frac{[a \sin(\theta/2) - b \cos(\theta/2)]}{\sin \theta} \\ &\quad - \frac{i[a-b - (2i+a+b)\cos \theta]}{(2i+a+b) \cdot \sin \theta}, \end{aligned} \quad (\text{A31a})$$

$$\begin{aligned} g^{i-1}(x) &= \left[\frac{(2i+a+b+1)}{(2i+a+b-1)} \frac{i(i+a+b)}{(i+a)(i+b)} \right]^{1/2} \\ &\quad \times \frac{2(i+a)(i+b)}{(2i+a+b) \cdot \sin \theta}. \end{aligned} \quad (\text{A31b})$$

The corresponding DVR matrix is again obtained by orthogonal transformation. The kinetic-energy matrix in the FBR, \mathbf{L}^R , is diagonal,

$$\mathbf{L}_{i'i}^R \equiv \int_{R_i}^{R_{i'}} \mathcal{F}_{i'}(R) \cdot \frac{-\partial^2 \mathcal{F}_i(R)}{\partial R^2} dR = {}^R d_i \cdot \delta_{i'i}, \quad (\text{A32})$$

from which the \mathbf{K}^R matrix of Eq. (14a) is evaluated using the transformation matrix defined in Eq. (13).

$$\mathbf{K}^R = (\mathbf{t}^R)^T \cdot \mathbf{L}^R \cdot \mathbf{t}^R. \quad (\text{A33})$$

APPENDIX B: NATURAL EXPANSION ANALYSIS

The natural expansion (NE) analysis provides a method for evaluating mode separability in a given coordinate system of multimode vibrational wave functions.³⁹⁻⁴¹ Separability of a particular mode from all the other modes is analyzed from the wave function of a given eigenstate. According to Eq. (16) in Sec. (II C), an eigenvector of the 3D Hamiltonian in DVR may be written as

$$\Psi(R, \theta, r) = \sum_{\alpha\beta\gamma} C_{\alpha\beta\gamma} \chi_{\alpha\beta\gamma}(R, \theta, r), \quad (\text{B1})$$

in which $\{C_{\alpha\beta\gamma}\}$ are the expansion coefficients, and $\{\chi_{\alpha\beta\gamma}\}$ are the direct product basis given in Eq. (7),

$$\chi_{\alpha\beta\gamma}(R, r, \theta) = \Gamma_{\alpha}(R) \cdot \Phi_{\beta}(r) \cdot \Theta_{\gamma}^{(a,b)}(x).$$

In order to evaluate mixing of the R coordinate with the (θ, r) coordinates, the natural expansion of the eigenfunction given by

$$\Psi[R, (\theta, r)] = \sum_q d_q F_q(R) \cdot G_q(\theta, r) \quad (\text{B2})$$

is obtained as follows. Since the G are orthonormal over (θ, r) , the density kernel \mathcal{P} for the coordinate R is defined for a given state is given by

$$\mathcal{P}(R, R') = \sum_{\alpha, \alpha'} \mathbf{A}_{\alpha'\alpha} \Gamma_{\alpha'}^*(R') \cdot \Gamma_{\alpha}(R) \quad (\text{B3a})$$

$$= \sum_q d_q^2 F_q^*(R') \cdot F_q(R), \quad (\text{B3b})$$

in which the matrix \mathbf{A} has been diagonalized to find eigenvalues, $\{d_q^2\}$, and $\{F_q\}$ are the optimized natural basis in the R coordinate for the specific vibrational state. $\mathbf{A}_{\alpha\alpha'}$ is defined in terms of the DVR expansion coefficients:

$$\mathbf{A}_{\alpha'\alpha} = \sum_{\beta} \sum_{\gamma} C_{\alpha\beta\gamma} C_{\alpha'\beta\gamma}. \quad (\text{B4})$$

From the equality between Eqs. (B3a) and (B3b), it can be deduced that

$$\mathbf{A}_{\alpha'\alpha} = \sum_q D_{q\alpha} D_{q\alpha'} \cdot d_q^2 \quad (\text{B5})$$

and

$$F_q(R) = \sum_{\alpha} D_{q\alpha} \Gamma_{\alpha}(R). \quad (\text{B6})$$

$\{F_q\}$ natural orbitals are the linear combination of DVR basis. Thus, $\{d_q^2\}$ are the eigenvalues of the matrix \mathbf{A} , denoting the population probabilities for dominant configurations. Since \mathbf{A} is a unitary matrix, $\sum_q \{d_q^2\} = 1$. $d_1 > 1/2$ implies an existence of one dominant configuration, and as $d_1 \rightarrow 1$ the R coordinate is completely uncoupled from the other two modes.

- ¹C. Camy-Peyret and J. M. Flaud, *Mol. Phys.* **32**, 523 (1976).
- ²J. M. Flaud, C. Camy-Peyret, and R. A. Toth, *International Tables of Selected Constants* (Pergamon, New York, 1981), Chap. 19.
- ³N. F. Scherer and A. H. Zewail, *J. Chem. Phys.* **87**, 97 (1987).
- ⁴A. R. Hoy, I. M. Mills, and G. Strey, *Mol. Phys.* **24**, 1265 (1972).
- ⁵Z. Bačić and J. C. Light, *J. Chem. Phys.* **85**, 4594 (1986).
- ⁶J. R. Henderson and J. Tennyson, *Mol. Phys.* **69**, 639 (1990).
- ⁷Z. Bačić and J. C. Light, *J. Chem. Phys.* **6**, 3065 (1987).
- ⁸M. Mladenovic and Z. Bačić, *J. Chem. Phys.* **93**, 3039 (1990).
- ⁹Robert M. Whitnell and J. C. Light, *J. Chem. Phys.* **90**, 1774 (1989).
- ¹⁰S. Carter and W. Meyer, *J. Chem. Phys.* **93**, 8902 (1990).
- ¹¹P. Bartlett and B. J. Howard, *Mol. Phys.* **70**, 1001 (1990).
- ¹²P. N. Day and D. G. Truhlar, *J. Chem. Phys.* **95**, 6615 (1991).
- ¹³Z. Bačić and J. Z. H. Zhang, *J. Chem. Phys.* **96**, 3707 (1992).
- ¹⁴J. R. Henderson, J. Tennyson, and B. T. Sutcliffe, *J. Chem. Phys.* **96**, 2426 (1992).
- ¹⁵D. O. Harris, G. G. Engerholm, and W. D. Gwinn, *J. Chem. Phys.* **43**, 151 (1965).
- ¹⁶A. S. Dickinson and P. R. Certain, *J. Chem. Phys.* **49**, 4209 (1968).
- ¹⁷J. V. Lill, G. A. Parker, and J. C. Light, *Chem. Phys. Lett.* **89**, 483 (1982).
- ¹⁸J. C. Light, I. P. Hamilton, and J. V. Lill, *J. Chem. Phys.* **82**, 1400 (1985).
- ¹⁹Per Jensen, *J. Mol. Spectrosc.* **133**, 438 (1989).
- ²⁰C. Camy-Peyret, J. M. Flaud, J. Y. Mandin, J. P. Chevillard, J. Brault, D. A. Ramsay, M. Vervloet, and J. Chauville, *J. Mol. Spectrosc.* **113**, 208 (1985).
- ²¹Bruce R. Johnson and William P. Reinhardt, *J. Chem. Phys.* **85**, 4538 (1986).
- ²²B. T. Sutcliffe, *Understanding Molecular Properties*, edited by J. Avery *et al.* (Reidel, Dordrecht, 1987), pp. 449-463.
- ²³Seung E. Choi and J. C. Light, *J. Chem. Phys.* **92**, 2129 (1990).
- ²⁴S. Carter and N. C. Handy, *Mol. Phys.* **57**, 175 (1986).
- ²⁵G. D. Carney, L. A. Curtiss, and S. R. Langhoff, *J. Mol. Spectrosc.* **61**, 371 (1976).
- ²⁶G. Simons, R. G. Parr, and J. M. Finlan, *J. Chem. Phys.* **59**, 3229 (1973).
- ²⁷W. Meyer, P. Botschwina, and P. G. Burton, *J. Chem. Phys.* **84**, 891 (1986).
- ²⁸Lauri Halonen and Tucker Carrington, Jr., *J. Chem. Phys.* **88**, 4171 (1988).
- ²⁹J. C. Light, R. M. Whitnell, T. J. Park, and S. E. Choi, "Quantum Dynamics of Small Systems Using Direct Variable Representations," in *Supercomputer Algorithms for Reactivity, Dynamics, and Kinetics of Small Molecules*, edited by A. Lagana, NATO ASI Series C, Vol. 277 (Kluwer, Dordrecht, 1989), p. 187.
- ³⁰Z. Bačić and J. C. Light, *Annu. Rev. Phys. Chem.* **40**, 469 (1989).
- ³¹Michael J. Davis, *J. Phys. Chem.* **92**, 3124 (1988).
- ³²J. A. Fernley, S. Miller, and J. Tennyson, *J. Mol. Spectrosc.* **150**, 597 (1991).
- ³³K. K. Lehmann, *J. Chem. Phys.* **79**, 1098 (1983).
- ³⁴K. K. Lehmann, *Mol. Phys.* **66**, 1129 (1989).
- ³⁵M. E. Kellman and L. Xiao, *Chem. Phys. Lett.* **162**, 486 (1989).
- ³⁶I. M. Mills and A. G. Robiette, *Mol. Phys.* **56**, 743 (1985).
- ³⁷M. S. Child and L. Halonen, *Adv. Chem. Phys.* **57**, 1 (1984).
- ³⁸L. Halonen and A. G. Robiette, *J. Chem. Phys.* **84**, 6861 (1986).
- ³⁹N. Moiseyev and R. E. Wyatt, *Chem. Phys. Lett.* **132**, 396 (1986).
- ⁴⁰N. Moiseyev, R. Schatzberger, P. Froelich, and O. Goscinski, *J. Chem. Phys.* **83**, 3924 (1985).
- ⁴¹N. Moiseyev, R. C. Brown, R. E. Wyatt, and E. Tzidon, *Chem. Phys. Lett.* **127**, 37 (1986).
- ⁴²G. Arfken, *Mathematical Methods for Physicists* (Academic, New York, 1985).